2010-11

Effect of different solvent ratios (water/ethylene glycol) on the growth process of CaMo'O IND.4' crystals and their optical properties

Crystal Growth and Design,Washington, DC : American Chemical Society - ACS,v. 10, n. 11, p. 4752-4768, Nov. 2010

http://www.producao.usp.br/handle/BDPI/49811

DOI: 10.1021/cg100584b

CRYSTAL GROWTH & DESIGN Article

2010, Vol. 10
4752–4768

Effect of Different Solvent Ratios (Water/Ethylene Glycol) on the Growth Process of $CaMoO_4$ Crystals and Their Optical Properties

V. S. Marques,[†] L. S. Cavalcante,*[,‡] J. C. Sczancoski,[§] A. F. P. Alcântara,[†] M. O. Orlandi,[‡] E. Moraes,[§] E. Longo,[‡] J. A. Varela,[‡] M. Siu Li,[∥] and M. R. M. C. Santos[†]

[†]*LIMAV-CCN-Química, UFPI—Universidade Federal do Piauí, 64049-550 Teresina, PI, Brazil,*
[‡]*UNESP—Universidade Estadual Paulista, P.O. Box 355, 14801-907 Araraquara, SP, Brazil,*
[§]*LIEC—Universidade Federal de São Carlos, P.O. Box 676, 13565-905 São Carlos, SP, Brazil, and*
[∥]*IFSC, Universidade de São Paulo, P.O. Box 369, 13560-970 São Carlos, SP, Brazil*

Received April 30, 2010; Revised Manuscript Received August 26, 2010

ABSTRACT: In this paper, calcium molybdate ($CaMoO_4$) crystals (meso- and nanoscale) were synthesized by the coprecipitation method using different solvent volume ratios (water/ethylene glycol). Subsequently, the obtained suspensions were processed in microwave-assisted hydrothermal/solvothermal systems at 140 °C for 1 h. These meso- and nanocrystals processed were characterized by X-ray diffraction (XRD), Fourier transform Raman (FT-Raman), Fourier transform infrared (FT-IR), ultraviolet−visible (UV−vis) absorption spectroscopies, field-emission gun scanning electron microscopy (FEG-SEM), transmission electron microscopy (TEM), and photoluminescence (PL) measurements. XRD patterns and FT-Raman spectra showed that these meso- and nanocrystals have a scheelite-type tetragonal structure without the presence of deleterious phases. FT-IR spectra exhibited a large absorption band situated at around 827 cm^{-1}, which is associated with the Mo−O antisymmetric stretching vibrations into the [MoO_4] clusters. FEG-SEM micrographs indicated that the ethylene glycol concentration in the aqueous solution plays an important role in the morphological evolution of $CaMoO_4$ crystals. High-resolution TEM micrographs demonstrated that the mesocrystals consist of several aggregated nanoparticles with electron diffraction patterns of monocrystal. In addition, the differences observed in the selected area electron diffraction patterns of $CaMoO_4$ crystals proved the coexistence of both nano- and mesostructures. First-principles quantum mechanical calculations based on the density functional theory at the B3LYP level were employed in order to understand the band structure and density of states for the $CaMoO_4$. UV−vis absorption measurements evidenced a variation in optical band gap values (from 3.42 to 3.72 eV) for the distinct morphologies. The blue and green PL emissions observed in these crystals were ascribed to the intermediary energy levels arising from the distortions on the [MoO_4] clusters due to intrinsic defects in the lattice of anisotropic/isotropic crystals.

Introduction

Calcium molybdate ($CaMoO_4$) is an important material belonging to the scheelite family with tetragonal structure and space group $I4_1/a$.[1,2a,b] In this structure, the Mo atoms are bonded to four oxygens, forming the [MoO_4] clusters, while the Ca atoms are coordinated to eight oxygens, forming the [CaO_8] clusters.[3−7] In recent years, this molybdate has attracted the attention of diverse scientific and technological fields because of its wide potential for applications in acousto-optic filters,[8] solid state lasers,[9,10] white light-emitting diodes,[11] scintillators,[12] microwave dielectrics,[13,14] fluorescent lamps,[15] negative electrodes for Li^+-ion batteries,[16] and cryogenic scintillation detectors for search of ^{100}Mo double β decay,[17,18] catalytic properties of propane ammoxidation,[19] and so on.

In terms of optical properties, this material exhibits green and/or blue luminescence emissions at room temperature when excited with wavelengths in the range from 240 to 537 nm.[19−22] However, few works in the literature have reported on the origin of the photoluminescence (PL) properties of $CaMoO_4$. For example, Mikhailik et al.[23] explained that the short wavelength luminescence of this molybdate is usually caused by the intrinsic emission of the MoO_4^{2-} molecular complexes while its long wavelength luminescence arises from the MoO_3 oxygen-deficient defect centers. In another work, Mikhailik et al.[24] investigated the electronic transitions and luminescence decay kinetics of $CaMoO_4$ at low temperatures (from −265 to 27 °C) by means of ultraviolet excitation. According to these authors, the optical transitions occur in the MoO_4^{2-} molecular complexes, mainly involving the ($^1A_1$) ground, singlet ($^1T^1$, $^1T_2$), and triplet ($^3T_1$, $^3T_2$) levels. In this case, the electric dipole allowed $^1A_1 \rightarrow {}^1T_2$ transitions contribute to the excitation process while the radiative transitions arise from the closely located lower-lying triplet states. Ryu et al.[25] mentioned that, besides the charge-transfer transitions within the MoO_4^{2-} complexes, the PL response can be influenced by morphology and particle size distribution. Marques et al.[26] attributed the origin of this optical property to the degree of structural order−disorder in the lattice. Recently, Longo et al.,[27] through the first-principles quantum mechanical calculations based on the density functional theory, reported that the green and blue PL emissions of disordered $CaMoO_4$ powders are linked to the intrinsic slight distortion of the [MoO_4] tetrahedral clusters.

Considering the different chemical routes, the conventional hydrothermal systems are well-known due to their versatility in the formation and crystallization of ceramic oxides at low temperatures, enabling a good control of morphologies and particle sizes.[28] On the other hand, the long processing times exhibited by this synthesis method were overcome using microwave radiation as energy source for this system. This innovation resulted in the development of equipment currently known as microwave-hydrothermal.[28] In order to obtain a good

*To whom correspondence should be addressed. E-mail: laeciosc@bol.com.br.

 Published on Web 10/01/2010

efficiency of the microwave radiation with the liquid phase, it is necessary to use substances or solvents with high dielectric loss (tan δ).[29] In addition, according to Thongtem et al.,[29] compounds with large permanent dipole moments have large dielectric constants or relative permittivities. During the interaction with the microwave radiation, these dielectric properties can be considered key factors to get a faster heating to high temperatures at short times. Hence, solutions in water (dielectric constant at 25 °C = 78.4)[30] and ethylene glycol (dielectric constant at 25 °C = 40.3)[29] are good candidates in order to be employed in microwave-assisted equipment operating at the frequency 2.45 GHz. The combination of microwave irradiation with the hydrothermal process was named the "microwave-hydrothermal" (MH) process. Similarly, the combination of microwave irradiation with solvothermal (not using water as a solvent) processes can be termed "microwave-solvothermal" (MS) processes, respectively. In relation to the utilization of different solvent ratios (water/ethylene glycol) for the preparation of $CaMoO_4$ oriented aggregate crystals and meso- and nanocrystals processed in a microwave, there are no works so far reported in the literature.

Therefore, in this paper, we report on the synthesis of $CaMoO_4$ oriented aggregate crystals and meso- and nanocrystals by the coprecipitation method with different solvent ratios ($H_2O/C_2H_6O_2$) and processed in a microwave-assisted hydrothermal/solvothermal system at 140 °C for 1 h. These meso- and nanocrystals were analyzed by X-ray diffraction (XRD), Fourier transform Raman (FT-Raman), Fourier transform infrared (FT-IR), ultraviolet−visible (UV−vis) absorption spectroscopies, field-emission gun scanning electron microscopy (FEG-SEM), transmission electron microscopy (TEM), and photoluminescence (PL) measurements. Also, the experimental data were correlated with those obtained by the first-principles quantum mechanical calculations. The electronic structure (band structure and density of states) was theoretically calculated. The main aim is to understand the effect of different solvent ratios ($H_2O/C_2H_6O_2$) in volume on the growth process of $CaMoO_4$ crystals and its influence on the optical properties.

Experimental Procedure

Synthesis and Microwave Processing of $CaMoO_4$ Crystals. The $CaMoO_4$ meso- and nanocrystals were synthesized by the coprecipitation method with different ratios of deionized water [H_2O] and ethylene glycol [$C_2H_6O_2$] (99.5% purity, J.T. Baker) and processed in a microwave-assisted hydrothermal/solvothermal system. The typical experimental procedure is described as follows: 0.0025 mol of molybdic acid [H_2MoO_4] (85% purity, Aldrich) and 0.0025 mol of calcium acetate monohydrate [$Ca(CH_3CO_2)_2 \cdot H_2O$] (99.5% purity, Aldrich) were added and dissolved in mixtures containing different solvent ratios (100 mL of H_2O; 75 mL of H_2O/25 mL of $C_2H_6O_2$; 50 mL of H_2O/50 mL of $C_2H_6O_2$; 25 mL of H_2O/75 mL of $C_2H_6O_2$ and 100 mL of $C_2H_6O_2$) in volume total. In the precipitation reaction, Ca^{2+} cations are the electron pair acceptor (Lewis acid), while the MoO_4^{2-} anions are the electron pair donor (Lewis base). The chemical reaction between these two species in solutions with different quantities of solvents (H_2O and $C_2H_6O_2$) results in formation of $CaMoO_4$, as shown below:

$$H_2MoO_4(s) + Ca(CH_3CO_2)_2 \cdot H_2O(s) \rightarrow 2H^+(aq) + 2CH_3CO_2^-(aq) + Ca^{2+}(aq) + MoO_4^{2-}(aq) \quad (1)$$

$$2H^+(aq) + 2CH_3CO_2^-(aq) \rightleftarrows 2CH_3COOH(aq) \quad (2)$$

$$Ca^{2+}(aq) + MoO_4^{2-}(aq) \rightarrow CaMoO_4(s)\downarrow \quad (3)$$

In order to increase the ionization rate, the solution pH was adjusted up to 10 by the addition of 5 mL of ammonium hydroxide [NH_4OH] (30% in NH_3, Mallinckrodt). In the sequence, these aqueous solutions with ethylene glycol, which has high affinity and solubility, due to formation of hydrogen bridges with water, were stirred for 30 min at room temperature. After the coprecipitation reaction, the solution was transferred into a Teflon autoclave, which was sealed and placed inside the microwave system (2.45 GHz, maximum power of 800 W). More details on this equipment have been reported in ref 31. All these systems were processed at 140 °C for 1 h. The heating rate in this system was fixed at 25 °C/min, and the pressure in the autoclave was stabilized at 294 kPa. After processing, the autoclave was naturally cooled to room temperature. The resulting suspension was washed with deionized water several times to neutralize the solution pH (≈7). Finally, the white precipitates were collected and dried in a conventional furnace at 65 °C for some hours.

Characterization of $CaMoO_4$ Crystals. The $CaMoO_4$ crystals were structurally characterized by X-ray powder diffraction (XRD) using a Rigaku-DMax/2500PC (Japan) with Cu Kα radiation (λ = 1.5406 Å) in the 2θ range from 5° to 75° with a scanning rate of 0.2°/s. FT-Raman spectroscopy was recorded with a Bruker-RFS 100 (Germany). The spectra were obtained using a 1064 nm line of a Nd:YAG laser, keeping its maximum output power at 110 mW. FT-IR spectroscopies were performed in the range from 395 to 1000 cm^{-1}, using a Bruker-Equinox 55 (Germany) spectrometer in transmittance mode. The viscosity of solvents were estimated at room temperature using a rheometer (Brookfield DV-III Ultra, USA). Nitrogen adsorption/desorption isotherms and specific surface area were recorded with an ASAP 2000 Phys/Chemisorption unit (Micromeritics, USA). In addition, the BET method (Brunauer, Emmett, and Teller)[32] was employed to estimate the specific surface area. The morphologies were investigated through a FEG-SEM of Carl Zeiss, model Supra 35-VP (Germany), operated at 6 kV and with a transmission electron microscope (TEM), model CM200 (Philips, USA), operated at 200 kV. In the preparation of TEM samples, the obtained powders were first dispersed in acetone using an ultrasonic bath for 20 min. Afterward, the suspensions were deposited on the copper grids via fast immersion. The crystallographic organizations as well as growth directions of $CaMoO_4$ crystals were investigated by means of high resolution transmission electron microscopy (HR-TEM) and selected-area electron diffraction (SAED). UV−vis spectra were taken using a spectrophotometer of Varian, model Cary 5G (USA), in diffuse reflection mode. PL measurements were performed with a Monospec 27 monochromator of Thermal Jarrel Ash (USA) coupled to a R446 photomultiplier of Hamamatsu Photonics (Japan). A krypton ion laser of Coherent Innova 90K (USA) (λ = 350 nm) was used as an excitation source, keeping its maximum output power at 200 mW. All measurements were performed at room temperature.

Density Functional Theory for the Electronic Structure of $CaMoO_4$. The periodic density functional theory (DFT) calculations were performed with the Becke's three-parameter hybrid nonlocal exchange functional, combined with the Lee-Yang-Par gradient-corrected correlation function B3LYP, which has proven to be a very effective tool to deal with the present challenging problem. According to the literature,[35] the B3LYP functional is able to simulate the energetic, geometric, and electronic properties of materials with acceptable accuracy. In particular, considering the scheelite-type tetragonal structure, this functional has been successfully employed in investigations on the electronic structure.[27] In this work, the atomic centers were described by the following electronic basis sets: 86-511d3G for calcium, 311(d31)G for molybdenum, and 8-411d11G for oxygen atoms.[36] The electronic structures were calculated with the CRYSTAL06 software[37] using the numerical second derivatives of the total energies. The band structures were obtained for 200 $\vec{K}$ points along the high-symmetry paths on the adequate Brillouin zone. The density of states (DOS) was calculated through the electronic structure analyses. The band structures and DOS diagrams were modeled by the XCRYSDEN program.[38]

Results and Discussion

X-ray Diffraction Analyses. Figure 1 illustrates the XRD patterns and lattice parameter values of $CaMoO_4$ crystals

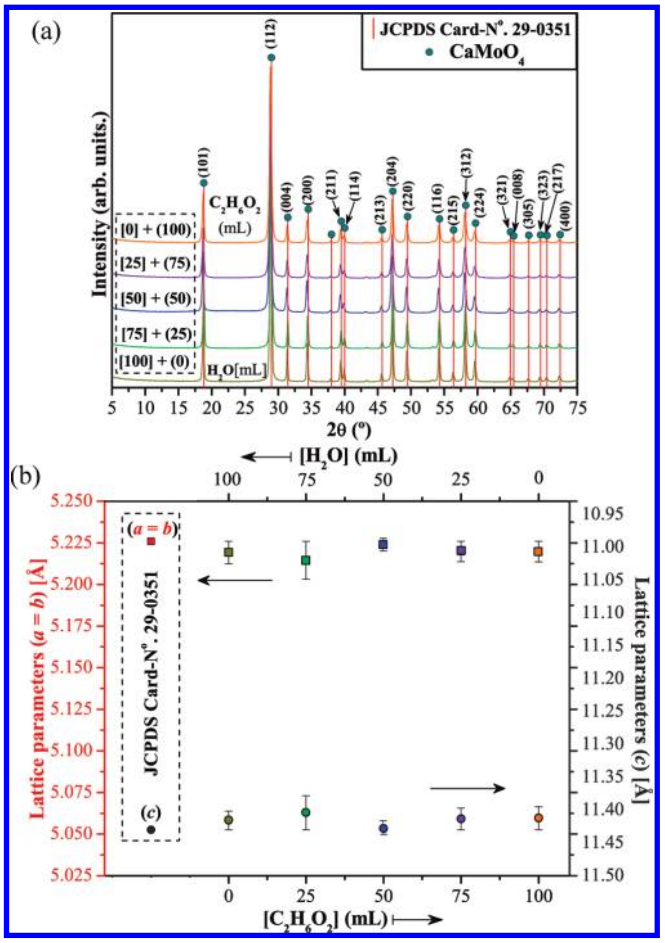

Figure 1. (a) XRD patterns of $CaMoO_4$ meso- and nanocrystals prepared with different solvent ratios ($H_2O/C_2H_6O_2$) and processed in a microwave-assisted hydrothermal/solvothermal system at 140 °C for 1 h and (b) $a = b$, and c lattice parameters as a function of different solvent ratios. The vertical bars show the standard mean error.

prepared with different solvent volume ratios ($H_2O/C_2H_6O_2$) and processed in a microwave-assisted hydrothermal/solvothermal system at 140 °C for 1 h, respectively.

All XRD patterns can be indexed to the tetragonal structure with space group $I4_1/a$, in agreement with the respective Joint Committee on Powder Diffraction Standards (JCPDS) No. 29-0351.[39] Diffraction peaks related to the secondary phases were not detected, indicating the formation of a pure-single phase. Also, it is possible to note that these peaks are intense and well-defined, suggesting a good degree of crystallization or structural ordering at long-range. The experimental lattice parameters and unit cell volume were calculated using the least-squares refinement from the UnitCell-97 program.[40] The obtained values are shown in Figure 1b and displayed in Table 1.

As can be seen in Figure 1b and Table 1, the lattice parameters and unit cell volume obtained in this work are very close to those reported in the literature[41−44] and with the respective JCPDS card No. 29-0351.[39] However, the slight variations or differences in these values can be directly related to the types of synthesis methods and experimental conditions (temperature, time, heating rate, atmosphere) as well as a consequence of the volumetric proportions ($H_2O/C_2H_6O_2$) in the nucleation or growth stages of the particles. Also, we demonstrate in previous papers that the lattice parameters are susceptible to modifications when there are residual stresses and/or distortions in the lattice.[45,46]

Representation of the $CaMoO_4$ Unit Cell. Figure 2 shows the schematic representation of the tetragonal $CaMoO_4$ unit cell with space group $I4_1/a$.

This ideal unit cell was modeled using the Java Structure Viewer Program (version 1.08lite for Windows) and VRML-View (version 3.0 for Windows)[47,48] by means of the atomic coordinates listed in Table 2. The $CaMoO_4$ crystals belong to the scheelite-type tetragonal structure (space group $I4_1/a$, No. 88, in the international tables of crystallography, and point-group symmetry C_{4h}^6).[49] In this structure, the molybdenum atoms are coordinated to four oxygens, forming $[MoO_4]$ clusters with tetrahedral configuration and tetrahedral polyhedra (4 vertices, 4 faces, and 6 edges).[50] These $[MoO_4]$ clusters are slightly distorted into the matrix, as a consequence of the O−Mo−O bond angles (108.3° and 111.8°), while the calcium atoms are bonded to eight oxygens, resulting in $[CaO_8]$ clusters with scalenohedral configuration and snub dispenoide polyhedra (8 vertices, 12 faces, and 18 edges).[51] For the construction of the unit cell, lattice parameters were used that showed the smallest deviations related to $CaMoO_4$ crystals prepared with 50 mL of H_2O and 50 mL of $C_2H_6O_2$. For visual effect, some bonds between the O−Ca−O and O−Mo−O atoms were highlighted in the unit cell.

Fourier Transform Raman/Infrared Spectroscopy Analyses. The group theory calculations showed the presence of 26 different vibrations for the $CaMoO_4$ crystals, which are represented by eq 4 below:[52,53]

$$\Gamma = 3A_g + 5A_u + 5B_g + 3B_u + 5E_g + 5E_u \quad (4)$$

where the A_g, B_g, and E_g are Raman-active vibration modes and the A and B modes are nondegenerate, while the E modes are doubly degenerate. The subscripts (g) and (u) indicate the parity under inversion in centrosymmetric $CaMoO_4$ crystals. The A_u and E_u modes correspond to the zero frequency of acoustic modes, while the others are optic modes. In addition, the A_g, B_g, and E_g modes arise from the same motion of the $CaMoO_4$ crystal. Therefore, 13 zone-center Raman-active modes are expected for the $CaMoO_4$, as presented by eq 5:[54,55]

$$\Gamma_{(\text{Raman})} = 3A_g + 5B_g + 5E_g \quad (5)$$

According to the literature,[56,57] the vibrational modes observed in Raman spectra of molybdates can be classified into two groups: external and internal modes. The vibrational external modes are related to the lattice phonon, which corresponds to the motion of $[CaO_8]$ clusters and the rigid cell units. The vibrational internal modes are correspondent to the vibration inside $[MoO_4]$ cluster units, considering the center of mass in the stationary state. In isolated $[MoO_4]$, tetrahedrons have a cubic symmetry point (T_d),[58] and its vibrations are composed of four internal modes ($\nu_1(A_1)$, $\nu_2(E_1)$, $\nu_3(F_2)$) and $\nu_4(F_2)$), one free rotation mode $\nu_{f.r.}(F_1)$, and one translation mode (F_2). On the other hand, when a $[MoO_4]$ tetrahedron is located in the scheelite structure, its point symmetry is reduced to S_4.[56]

In eq 5 the $1A_u$ and $1E_u$ are acoustic or infrared inactive modes, while those for 3Bu are forbidden infrared modes. In this situation, only eight infrared-active vibration modes remain, as presented by eq 6:[59,60]

$$\Gamma_{(\text{infrared})} = 4A_u + 4E_u \quad (6)$$

Figure 3 shows the FT-Raman spectra of $CaMoO_4$ crystals synthesized by the coprecipitation method with different

Table 1. Comparative Results between the Lattice Parameters and Unit Cell Volume of $CaMoO_4$ Obtained in This Work with Those Reported in the Literature by Different Synthesis Methods[a]

method	T (°C)	time (h)	lattice a	parameter b	c (Å)	unit cell volume (Å^3)	ref
MEHT	160	16	5.19	5.19	11.25	303.031	41
CZ	1200	24	5.1987	5.1987	11.4584	309.6802	42
CP	600	2	5.2231	5.2231	11.3973	310.9271	43
SSR	800	2	5.226	5.226	11.43	312.165	44
MH	140	1	5.219(2)	5.219(2)	11.415(8)	310.966(9)	[□]
MH	140	1	5.214(5)	5.214(5)	11.404(1)	310.088(9)	[□]
MSH	140	1	5.223(8)	5.223(8)	11.428(4)	311.859(1)	[□]
MS	140	1	5.219(8)	5.219(8)	11.413(5)	310.975(7)	[□]
MS	140	1	5.219(7)	5.219(7)	11.412(5)	310.936(6)	[□]
JCPDS			5.226	5.226	11.43	312.165(5)	39

[a] T = temperature, ref = references, MEHT = microemulsion-hydrothermal, CZ = Czochralski, CP = complex polymerization; SSR = solid state reaction; MH = microwave-hydrothermal, MHS = microwave-hydrothermal-solvothermal, MS = microwave-solvothermal, and [□] = this work.

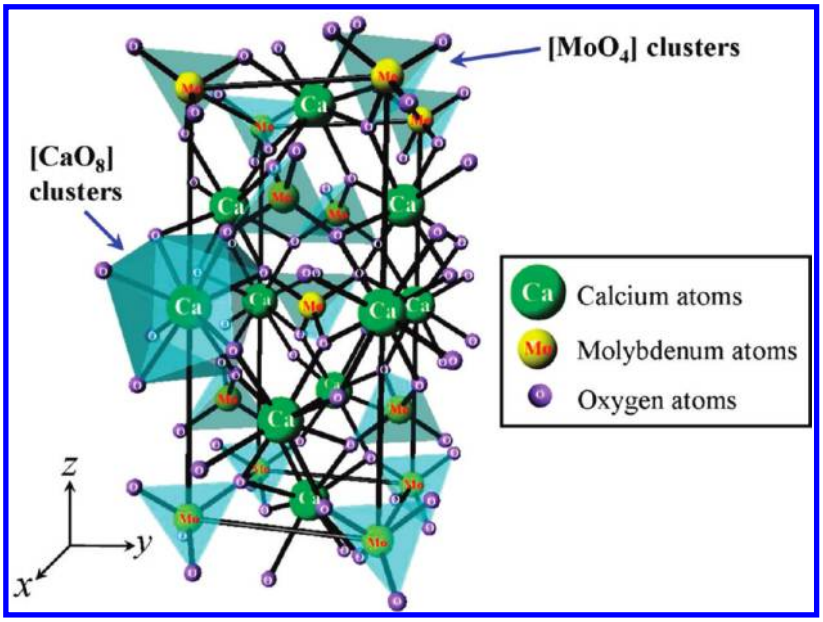

Figure 2. Schematic representation of the $CaMoO_4$ (1 × 1 × 1) unit cell illustrating the $[MoO_4]$ and $[CaO_8]$ clusters.

Table 2. Atomic Coordinates Employed To Model the $CaMoO_4$ Unit Cell[a]

atom	site	x	y	z
calcium	4b	0	0	0.5
molybdenum	4a	0	0	0
oxygen	16f	0.233	0.14	0.082

[a] $a = b = 5.224$ Å, $c = 11.428$ Å, $\alpha = \beta = \gamma = 90°$.

solvent volume ratios ($H_2O/C_2H_6O_2$) and processed in a microwave-assisted hydrothermal/solvothermal system at 140 °C for 1 h.

As can be illustrated in Figure 3, only 11 Raman-active modes were detected; the other ($1B_g$ and $1E_g$) vibration modes were not detectable, probably due to their low intensities. Moreover, the Raman spectra exhibited intense and sharp bands, indicating a strong interaction between the O−Ca−O and O−Mo−O bonds in the clusters.[60,61] In principle, this characteristic is normally observed in materials structurally ordered at short-range. The inset illustrates a typical $[MoO_4]$ cluster with symmetric stretching vibrations between the O−Mo−O bonds. The positions of each Raman-active mode are listed in Table 3.

A closer analysis of the results displayed in this table indicated that the relative positions of all Raman-active

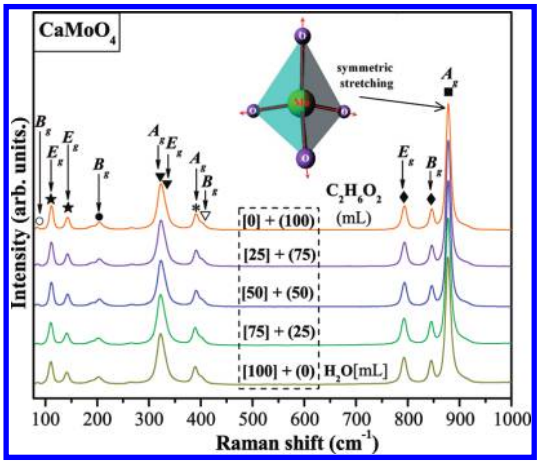

Figure 3. FT-Raman spectra in the range from 75 to 1000 cm^{-1} for the $CaMoO_4$ meso- and nanocrystals prepared with different solvent ratios ($H_2O/C_2H_6O_2$) and processed in a microwave-assisted hydrothermal/solvothermal system. The inset shows the $[MoO_4]$ clusters with symmetric stretching vibration.

modes of $CaMoO_4$ crystals reported in this work are in good agreement with those previously reported in the literature.[62−64] In fact, the shifts observed on these positions can be

Table 3. Comparative Results between the Experimental Raman-Active Modes of $CaMoO_4$ Obtained in This Work and Those Reported in the Literature by Different Synthesis Methods[a]

M	T (°C)	t (h)	B_g (○)	E_g (★)	E_g (★)	B_g (●)	A_g (▼)	E_g (▼)	A_g (∗)	B_g (▽)	E_g (♦)	B_g (♦)	A_g (■)	ref
CZ	1200	40		112	143	205	322	328	391	402	792	845	877	62
CZ	1200	24		111.5	143	204.5	321.5	327.5	391	402.5	792	845.5	877	63
CP	700	2	86	112	143	204	323		391	402	794	847	878	64
MH	140	1	83	110	141	203	322	324	391	401	793	845	878	[□]
MH	140	1	83	110	141	202	322	324	391	401	793	845	878	[□]
MHS	140	1	83	110	141	202	322	324	391	401	793	845	878	[□]
MS	140	1	83	110	141	201	322	324	390	401	793	845	878	[□]
MS	140	1	83	110	141	201	322	324	390	403	793	845	878	[□]

[a] Symbols in the column head correspond to the labeled peaks in Figure 3; M = method; T = temperature; t = time; Raman modes = (cm^{-1}); CZ = Czochralski; CP = complex polymerization; MH = microwave-hydrothermal, MHS = microwave-hydrothermal-solvothermal, MS = microwave-solvothermal, and [□] = this work.

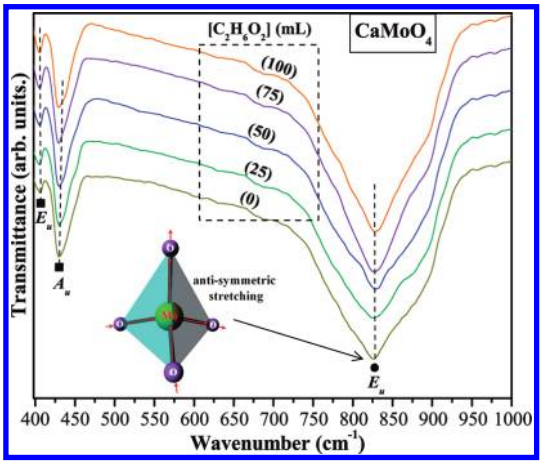

Figure 4. FT-IR spectra in the range from 395 to 1000 cm^{-1} for the $CaMoO_4$ meso- and nanocrystals prepared with different solvent ratios ($H_2O/C_2H_6O_2$) and processed in a microwave-assisted hydrothermal/solvothermal system. The inset shows the [MoO_4] clusters with antisymmetric stretching vibration.

correlated to the structural modifications induced by the synthesis methods, mainly including the following: distortions on the [MoO_4] clusters, the degree of interaction between the O−Mo−O bonds, and variations on the bond lengths, angles and/or symmetry break induced by the structural order−disorder in the lattice.

Figure 4 shows the FT-IR spectra of $CaMoO_4$ crystals synthesized by the coprecipitation method with different solvent volume ratios ($H_2O/C_2H_6O_2$) and processed in a microwave-assisted hydrothermal/solvothermal system at 140 °C for 1 h.

As was previously described in the text, the molybdates belonging to the scheelite group are able to present up to eight stretching and/or bending vibration modes in infrared spectra.[65,66] In our case, it was possible to identify no more than three of these modes ($1A_u$ and $2E_u$), which are found in specific positions in the spectra. First, the strong absorption band situated at 827 cm^{-1} (E_u mode) is related to the $\nu_3(F_2)$ internal mode originated from the antisymmetric stretching vibrations in the [MoO_4] clusters. The other two weak absorption bands located at 405 cm^{-1} (E_u mode) and 430 cm^{-1}(A_u mode) are generally associated with the $\nu_4(F_2)$ internal modes due to the presence of antisymmetric bending vibrations involved in the O−Mo−O bonds. The inset illustrates a characteristic [MoO_4] cluster with antisymmetric stretching vibrations.

Table 4 shows a comparison of the relative positions between the infrared-actives modes of $CaMoO_4$ obtained in this work with those reported in the literature.[64,67,68]

Table 4. Comparative Results between the Experimental Infrared Active Modes of $CaMoO_4$ Obtained in This Work and Those Reported in the Literature by Different Synthesis Methods[a]

M	T (°C)	t (h)	E_u (cm^{-1}) (■)	A_u (cm^{-1}) (■)	E_u (cm^{-1}) (●)	ref
CP	700	2		430	820	64
HT	120	72		428	821	67
SG	900	2		436	818	68
MH	140	1	407	430	827	[□]
MH	140	1	405	430	827	[□]
MHS	140	1	406	430	827	[□]
MS	140	1	405	430	827	[□]
MS	140	1	405	430	827	[□]

[a] ■ and ● correspond to the labeled peaks in Figure 4; M = method; T = temperature; t = time; CP = complex polymerization; HT = hydrothermal, SG = sol-gel; MH = microwave-hydrothermal, MHS = microwave-hydrothermal-solvothermal, MS = microwave-solvothermal, and [□] = this work.

There is a considerable shift in the position of these vibrations, as indicated in this table, mainly in those E_u modes. Taking into account this observation, this behavior is supposed to be related to the interaction forces between the O−Mo−O bonds and/or distortions on the [MoO_4] clusters in the lattice.

FEG-SEM Analyses of $CaMoO_4$ Crystals. Figure 5a−l shows the FEG-SEM micrographs of $CaMoO_4$ crystals prepared with different solvent volume ratios ($H_2O/C_2H_6O_2$) and processed in a microwave-assisted hydrothermal/solvothermal system at 140 °C for 1 h, respectively.

FEG-SEM micrographs were of fundamental importance to understanding the morphological evolution process of $CaMoO_4$ crystals with the variations in the solvent volume proportions. Figure 5a and b indicated the formation of a large quantity of corn-cob-like $CaMoO_4$ crystals for the synthesis performed only in aqueous solution. Clearly, it can be seen that these structures are essentially constituted of small aggregated particles with octahedral shape, which have been partially oriented and attached on the irregular faces (inset in Figure 5b). Under these conditions, it is possible to conclude that several nanocrystallites nucleate and grow into small seed particles. In order to minimize the overall energy of the system, a great number of these seed particles tend to aggregate together.[69−71]

In the synthesis containing 25 mL of $C_2H_6O_2$, the FEG-SEM micrographs confirmed the existence of two distinct types of microcrystals (corn cob and dumbbell shapes), as shown in Figure 5c−e. Gong et al.[41] and Chen et al.[72] explained that the formation of dumbbell-like morphologies is associated with the oriented aggregation mechanism, which involves the spontaneous self-organization of adjacent particles along a common crystallographic orientation. On the

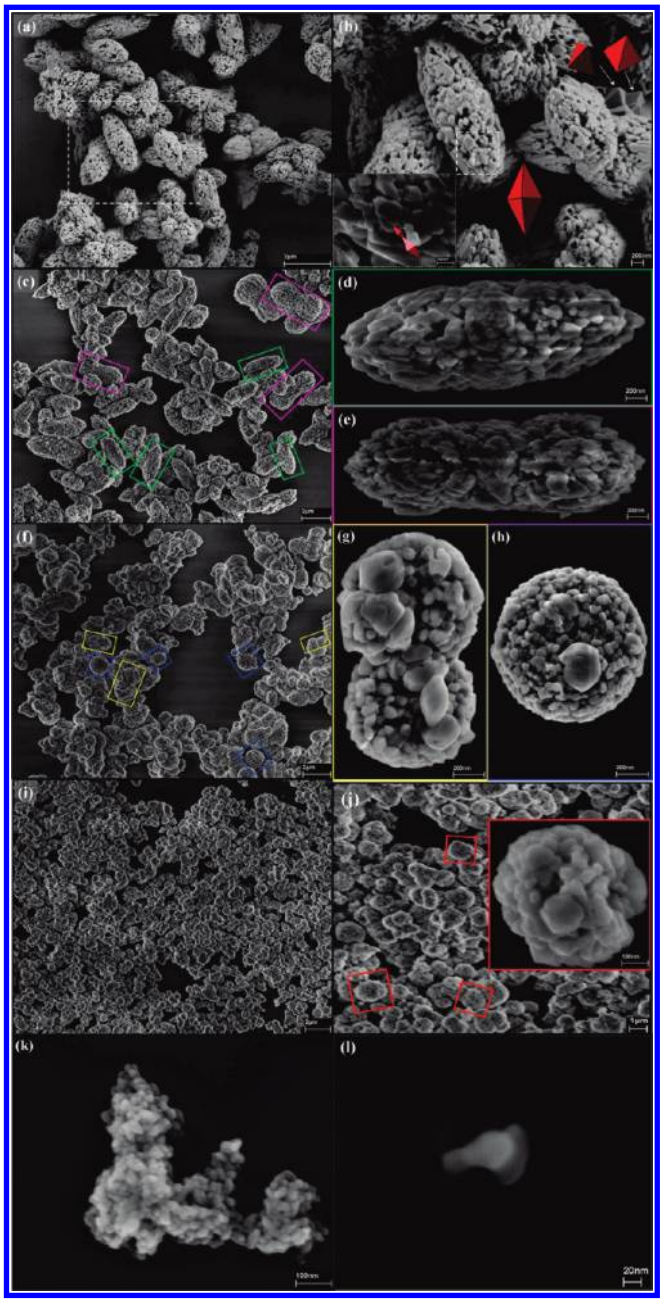

Figure 5. (a) Low magnification FEG-SEM micrograph of several $CaMoO_4$ crystals. (b) High magnification FEG-SEM micrographs of selected area in part a (dotted white square). Insert shows the zoom in part b of $CaMoO_4$ nanocrystals and nano-octahedrons with well-defined faces prepared with 100 mL of H_2O as solvent. (c) Low magnification FEG-SEM micrograph of several $CaMoO_4$ crystals prepared with 75 mL of H_2O and 25 mL of $C_2H_6O_2$ as solvents. Pink and green rectangles in part c are illustrated individually by high magnification FEG-SEM micrographs in parts d and e. (f) Low magnification FEG-SEM micrograph of several spherical-like $CaMoO_4$ mesocrystals prepared with 50 mL of H_2O and 50 mL of $C_2H_6O_2$ as solvents. Blue squares and yellow rectangles in part f are illustrated individually by high magnification FEG-SEM micrographs in parts g and h. (i) Low magnification FEG-SEM micrograph of several quasispherical-like $CaMoO_4$ nanostructures prepared with 25 mL of H_2O and 75 mL of $C_2H_6O_2$ as solvents. (j) Medium magnification FEG-SEM micrographs of quasi-spherical-like $CaMoO_4$ nanostructures. Inset in part j (red square) illustrates individual quasi-spherical-like $CaMoO_4$ nanostructures. (k) Low magnification FEG-SEM micrograph of several $CaMoO_4$ nanocrystals prepared with 100 mL of $C_2H_6O_2$ as solvent. (l) High magnification FEG-SEM micrographs of $CaMoO_4$ nanocrystals.

other hand, these authors explained that during the growth processes these structures are kinetically controlled by means of Ostwald ripening.

For the system containing the same volume of H_2O and $C_2H_6O_2$ (50 mL of each solvent), significant changes were noted with respect to the morphologic shapes. As can be seen in Figure 5f−h, the synthesis and MH processing conditions promoted the appearance of spherical-like $CaMoO_4$ mesocrystals. According to the literature,[73] the mesocrystals are classified as a new class of solid materials, which can be regarded as assemblies of crystallographically oriented nanocrystals with high crystallinity and porosity. Thus, the quantity of $C_2H_6O_2$ employed in this case was sufficient to inhibit the growth of anisotropic superstructures. In principle, we presume that the continuous adsorption and desorption processes of this organic polymeric compound during the MH processing and the strong interaction between the inorganic faces along preferential crystallographic directions enabled the origin of these mesostructures. Recently, Xu et al.[74] observed nanostructured $CaMoO_4$ microspheres by means of ionic liquid-assisted synthesis. These authors concluded that the ionic liquid acted as a structure-directing template or surfactant in the formation of these microspheres. The increase in the $C_2H_6O_2$ volume up to 75 mL caused a new modification of the particle morphologies. In the present case, the high concentration of $C_2H_6O_2$ in the aqueous solution has a tendency to limit the interaction between the small particles. As the adsorption and desorption processes on the surface of $CaMoO_4$ particles are not well-controlled during the MH processing, a random aggregation takes place, with a subsequent growth occurring via aggregation (Figure 5i and j).

The last synthesis, also known as the solvothermal synthesis, was simply performed with $C_2H_6O_2$, i.e., without the presence of H_2O. In this circumstance, the high viscosity of this polymeric substance is able to modify the mobility of the primary particles in suspension as well as its effective collision rates. Moreover, the predominance of $C_2H_6O_2$ in the solution implies a high adsorption of this compound on the inorganic surfaces, which is able to induce a steric hindrance, since this polymer surfactant (ethylene glycol) has a higher viscosity in relation to that of water (see Supporting Information Figure SI-1). Probably, this chemical event leads to a minimizing in the growth process, causing a reduction of the particle sizes. Afterward, as $C_2H_6O_2$ has good interaction with microwave radiation at frequencies of 2.45 GHz, it is acceptable that this physical phenomenon causes the presence of localized superheating in the liquid phase,[75−77] leading to a disordered aggregation or crystallographic fusion of the nanoparticles (Figure 5k and l). These nanocrystals present large surface area and N_2 absorption in relation to the case of oriented aggregate crystals (see Supporting Information Figures SI-2 and 3).

TEM Analyses of $CaMoO_4$ Crystals. Figure 6 shows the TEM/HR-TEM micrographs and SAED patterns of $CaMoO_4$ crystals prepared with different solvent volume ratios ($H_2O/C_2H_6O_2$) and processed in the microwave-assisted hydrothermal/solvothermal system at 140 °C for 1 h, respectively.

Figure 6a illustrates the low magnification TEM micrographs of corn-cob-like $CaMoO_4$ oriented aggregate crystals obtained only in the presence of H_2O (100 mL). In this micrograph, the dark areas are related to the high concentration of small octahedron-like particles with aggregate

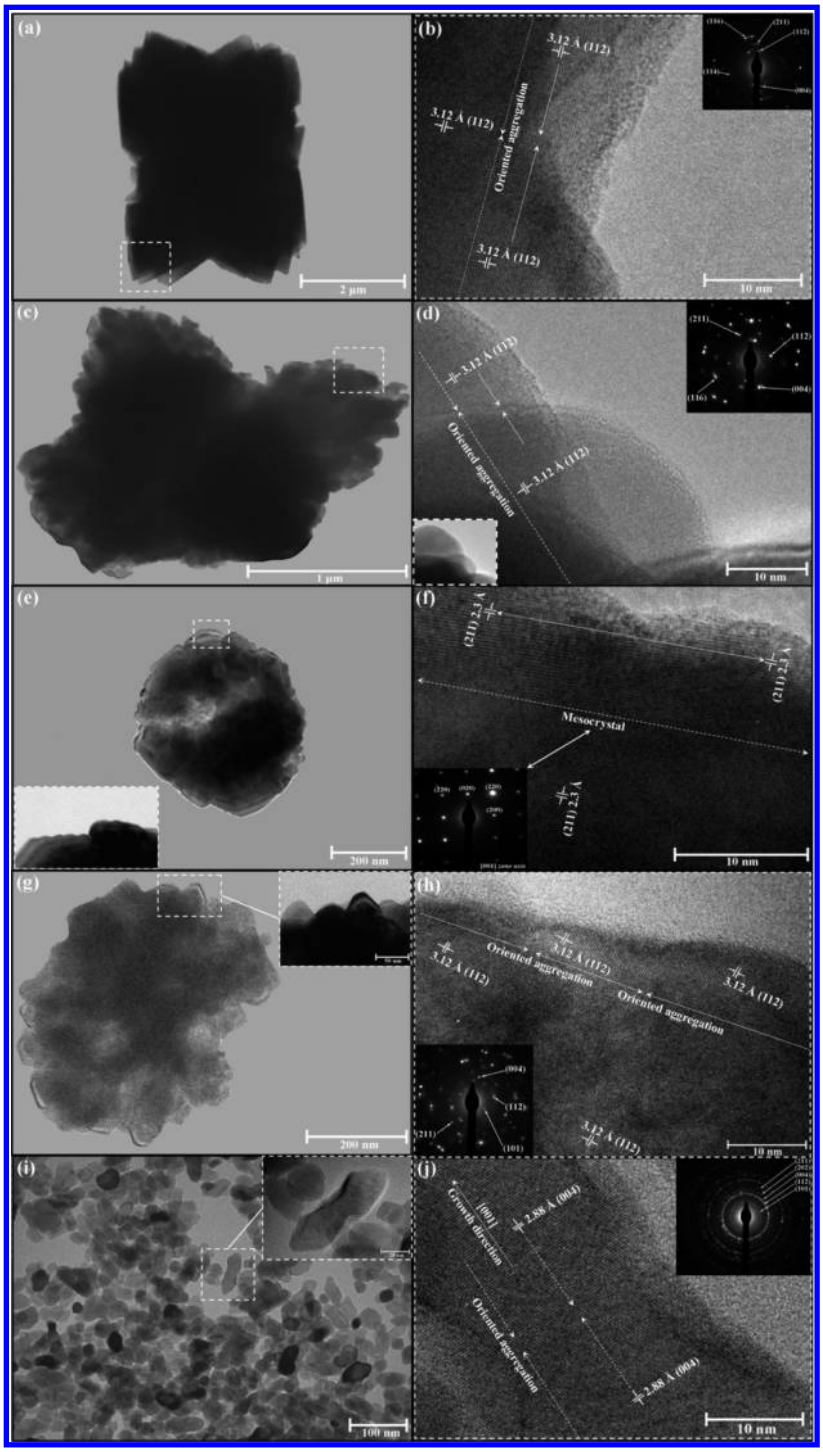

Figure 6. (a) Low magnification TEM micrographs of $CaMoO_4$ crystals synthesized in aqueous solution. (b) HR-TEM micrograph performed on the edge of a crystal (dotted white square) (inset shows the corresponding SAED pattern). (c) TEM micrographs of $CaMoO_4$ crystals synthesized with different solvent volume ratios: 75 mL of H_2O/25 mL of $C_2H_6O_2$. (d) HR-TEM micrograph performed on the edge of a crystal (dotted white square) (inset shows the corresponding SAED pattern). (e) TEM micrographs of $CaMoO_4$ mesocrystals synthesized with different solvent volume ratios: (50 mL of H_2O/50 mL of $C_2H_2O_2$. (f) HR-TEM micrograph performed on the edge of a mesocrystal (dotted white square) (inset shows the corresponding SAED pattern). (g) TEM micrographs of $CaMoO_4$ crystals synthesized with different solvent volume ratios: 25 mL of H_2O/75 mL of $C_2H_6O_2$. (h) HR-TEM micrograph performed on the edge of a crystal (dotted white square) (inset shows the corresponding SAED pattern). (i) TEM micrographs of $CaMoO_4$ crystals synthesized with 100 mL of $C_2H_6O_2$. (j) HR-TEM micrograph performed on the two nanocrystals when aggregation oriented (dotted white square) (inset shows the corresponding SAED pattern).

nature, confirming also that these microstructures are not internally hollow[78] (Figure 6a and Supporting Information Figure SI-4(a)). HR-TEM performed in the corner of these corn-cob-like morphologies (dashed white square in Figure 6a and b) revealed an oriented aggregation of two small particles exactly in the (112) plane, as estimated by the planar spacing of 3.12 Å. However, the SAED showed a characteristic polycrystalline diffraction pattern (inset Figure 6b), suggesting that the assemblies of particles were randomly organized in the formation stages of corn-cob-like

microcrystals (Supporting Information Figure SI-4(b-d)). Additionally, other TEM micrographs demonstrated that the growth occurs preferentially along the [001] direction. In principle, a more precise analysis of the TEM/HR-TEM micrographs and SAED data illustrated in Figure 6c and d suggested that the $CaMoO_4$ crystals obtained in the synthesis with 75 mL of H_2O have the same behavior as that of those specifically obtained in aqueous solution (Figure 6a and b; also see Supporting Information Figure SI-4(e,f)). As was expected, the spherical-like shapes are observed in the dark area in the TEM micrographs, signifying that these morphologies are constituted by a discrete accommodation of several particles. In contrast with the other obtained morphologies, the HR-TEM microscopy carried out on an exterior part showed a region with perfect attachment and alignment between two particles (Figure 6e and f). We presume that the growth process conducted by the microwave heating increased the effective collision rates, producing irreversible oriented attachments if the particles achieve a congruent alignment in the interface.[79] An important observation was possible through the HR-TEM and SAED techniques, where the chosen region (dashed white square and inset in Figure 6e) revealed that the attachments occurred in the (211) plane, according to the planar spacing of 2.3 Å (Figure 6f and Supporting Information Figures SI-4(g,h)). A significant point verified in the SAED was the evidence of a general single-crystal pattern for the octahedral-like crystal,[80,81] supporting the existence of mesostructures for this system formed with equivalent volume ratios (H_2O/$C_2H_6O_2$). Taking into consideration the solution composed of 25 mL of H_2O and 75 mL of $C_2H_6O_2$, the TEM images provided a possible random stacking of particles as shown in Figure 6g and supported by the FEG-SEM measurements (Figures 5i and 5j). In this system, the HR-TEM micrographs allowed us to assume that, after collision events, some particles tend to remain attached in compatible crystallographic planes. In the case illustrated in Figure 6h, the oriented aggregation happened along the (112) plane. On the other hand, the diffraction pattern obtained by the SAED technique in the selected fraction in Figure 6h (dashed white square) (see Supporting Information Figure SI-4(i,j)) confirmed that these morphologies do not have an analogous characteristic of microcrystals. A large polydisperse distribution of irregular nanoparticles was visualized in the TEM images (Figure 6i). Also, choosing some of these particles (dashed white square and inset in Figure 6i), the presence of oriented aggregation due to the junction detected in the interface contact between the nanoparticles was found by HR-TEM measurements (corresponding to a crystallographic distance of approximately 2.88 Å) (Figure 6j). As was presumed, this particle system has a polycrystalline behavior because of the different crystallographic orientations identified in the SAED patterns (Supporting Information Figure SI-4(k,l)). According to Yu et al.,[82] the morphological changes could be ascribed to selective interaction or adsorption of polymer molecules on certain crystal faces of scheelite, resulting in different modes of crystal growth along different crystallographic directions.

Average Size Distribution of $CaMoO_4$ Crystals. FEG-SEM micrographs were also of great importance to evaluate the average particle size distribution of different $CaMoO_4$ crystals obtained in this work. Hence, the counting of 100 crystals was performed to ensure a good statistic response (Figure 7).

In all cases, the counting of particle sizes was well-described by the log−normal distribution:

$$y = y_0 + \frac{A}{\sqrt{2\pi}wx} e^{-\left[\ln \frac{x}{x_c}\right]^2/2w^2} \quad (7)$$

where y_0 is the first value on the y-axis, A is the amplitude, w is the width, π is a constant, and x_c is the center value of the distribution curve on the x-axis.

The corn-cob-like $CaMoO_4$ crystals formed only in H_2O exhibited an average size distribution in the range from 1.25 to 4.75 μm (Figure 7a and inset). In this system, it was estimated that 35% of these structures have an average size of approximately 2.75 μm. The addition of 25 mL of $C_2H_6O_2$ into the aqueous solution (75 mL) resulted in two types of corn-cob-like crystals, where their sizes are situated in the range from 0.75 to 4.25 μm (Figure 7b and insets). As can be seen in Figure 7c, the $CaMoO_4$ mesocrystals presented an average size distribution from 0.5 to 1.9 μm; that is, 27% of these mesocrystals have an average size of 1.1 μm. The predominance of $CaMoO_4$ (75 mL) in the chemical synthesis promoted a reduction in the crystal size (from 0.475 to 0.825 μm) (Figure 7d and inset). In contrast, as was previously described in the text, the high adsorption of $C_2H_6O_2$ on the $CaMoO_4$ surfaces caused a significant morphologic change, i.e., inducing the formation of irregular nanoparticles with 35% of nanocrystals have an average size of 27.5 nm (Figure 7e and inset).

Growth Mechanism of $CaMoO_4$ Crystals. Figure 8 shows a schematic representation of all stages involved in the synthesis and growth mechanism of $CaMoO_4$ crystals synthesized by the coprecipitation method at room temperature and processed in a microwave-assisted hydrothermal/solvothermal system at 140 °C for 1 h.

Figure 8a illustrates the initial synthesis method, with the addition of stoichiometric amounts of respective reagents [H_2MoO_4 and $Ca(CH_3CO_2)_2 \cdot H_2O$]. In order, these reagents were dissolved in deionized water under constant stirring. In this solution, the energy of solvation of H_2O molecules promotes rapid salt dissociation and acid ionization, where the Ca^{2+} and MoO_4^{2-} ions are quickly solvated by H_2O molecules. The partial negative charges on the H_2O molecules are electrostatically attracted by Ca^{2+} ions, while the partial positive charges on the H_2O molecules are electrostatically attracted by MoO_4^{2-} ions (inset of Figure 8a). However, due to the difference of the electronic density of the Ca^{2+} and MoO_4^{2-} ions, a strongest force electrostatic attraction occurs between both, resulting in the formation of the first $CaMoO_4$ precipitates. In the following, the precipitation rate was increased by the addition of 5 mL of NH_4OH into this solution (Figure 8b). Also, in this same figure, we can note that the presence of different solvent ratios (H_2O/$C_2H_6O_2$) can lead to several possibilities of intermolecular interactions (hydrogen bonding). In the first case, the interactions between the H_2O molecules are stronger due to hydrogen bonds and the difference of electronegativity between atoms (H and O). These create highly polar bonds with hydrogen, which leads to strong bonding between hydrogen atoms (H δ^+) on one molecule and the lone pairs of oxygen atoms (O δ^-) on adjacent H_2O molecules.[83−85] It is verified that each H_2O molecule can potentially form four hydrogen bonds with surrounding H_2O molecules. There are exactly a sure number of δ^+ hydrogens and lone pairs so that every one of them can be involved in hydrogen bonding.[86] In the second case, the presence of hydrogen bonding for the

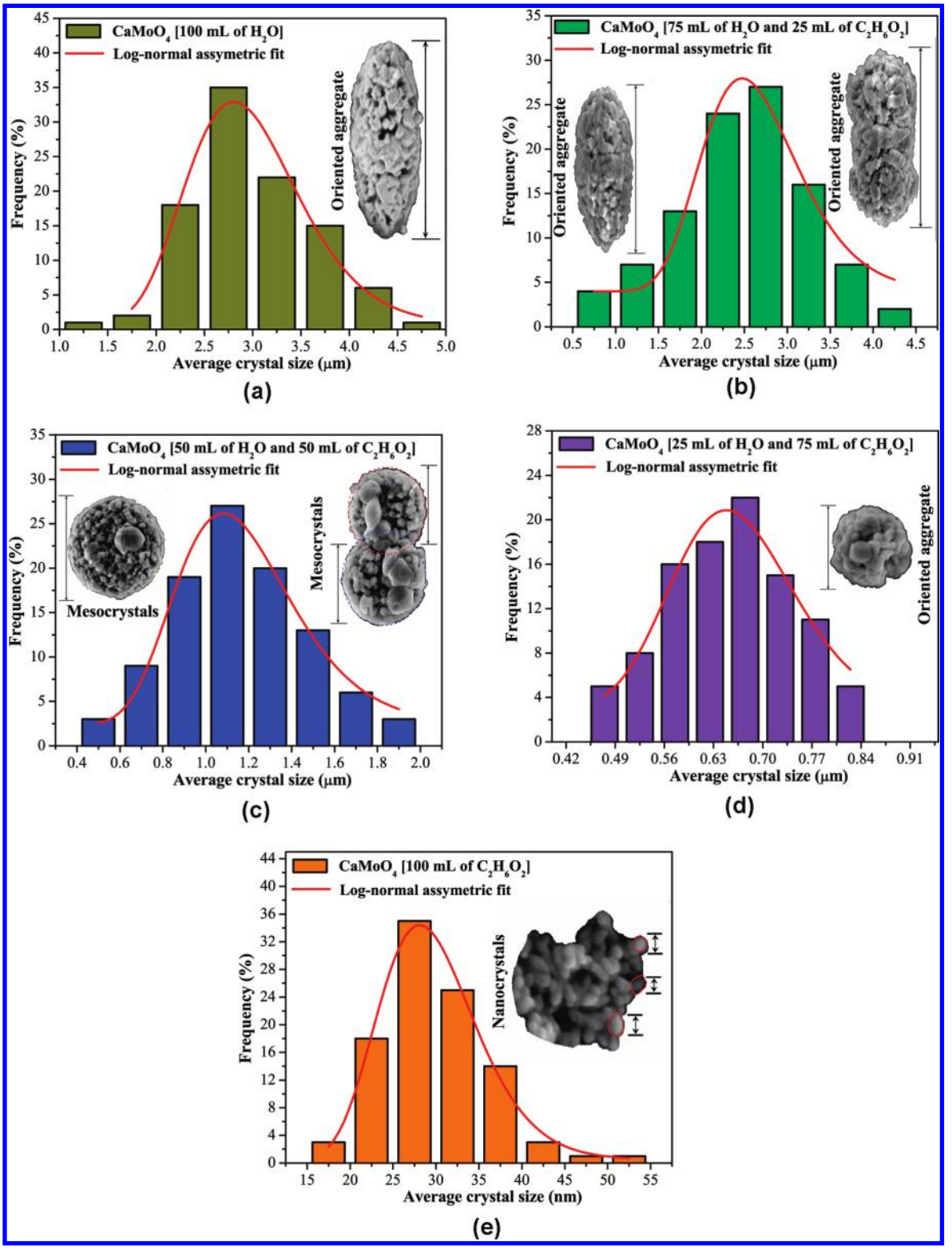

Figure 7. Average size distribution of $CaMoO_4$ meso- and nanocrystals prepared with different solvent ratios ($H_2O/C_2H_6O_2$) and processed in a microwave-assisted hydrothermal/solvothermal system: (a) 100 mL of H_2O, (b) 75 mL of H_2O and 25 mL of $C_2H_6O_2$, (c) 50 mL of H_2O and 50 mL of $C_2H_6O_2$, (d) 25 mL of H_2O and 75 mL of $C_2H_6O_2$, and (e) 100 mL of $C_2H_6O_2$.

system also is noted (ethylene glycol and water), and each ethylene glycol molecule can potentially form four hydrogen bonds with surrounding H_2O molecules.[71] In the third case, also we observed the presence of hydrogen bonding between the ethylene glycol, and its hydrophilic characteristics are due to hydrogen bonds among the OH bonds.[87] In ethylene glycol molecules, each pair of OH groups is able to form hydrogen bonding with other OH groups, due to a difference of electronegativity between the atoms (O δ^- and H δ^+); thus, this chemical bond presents a certain polarity.[88,89] In Figure 8c, the effect of solvent ratios on the processing of $CaMoO_4$ oriented aggregate crystals and meso- and

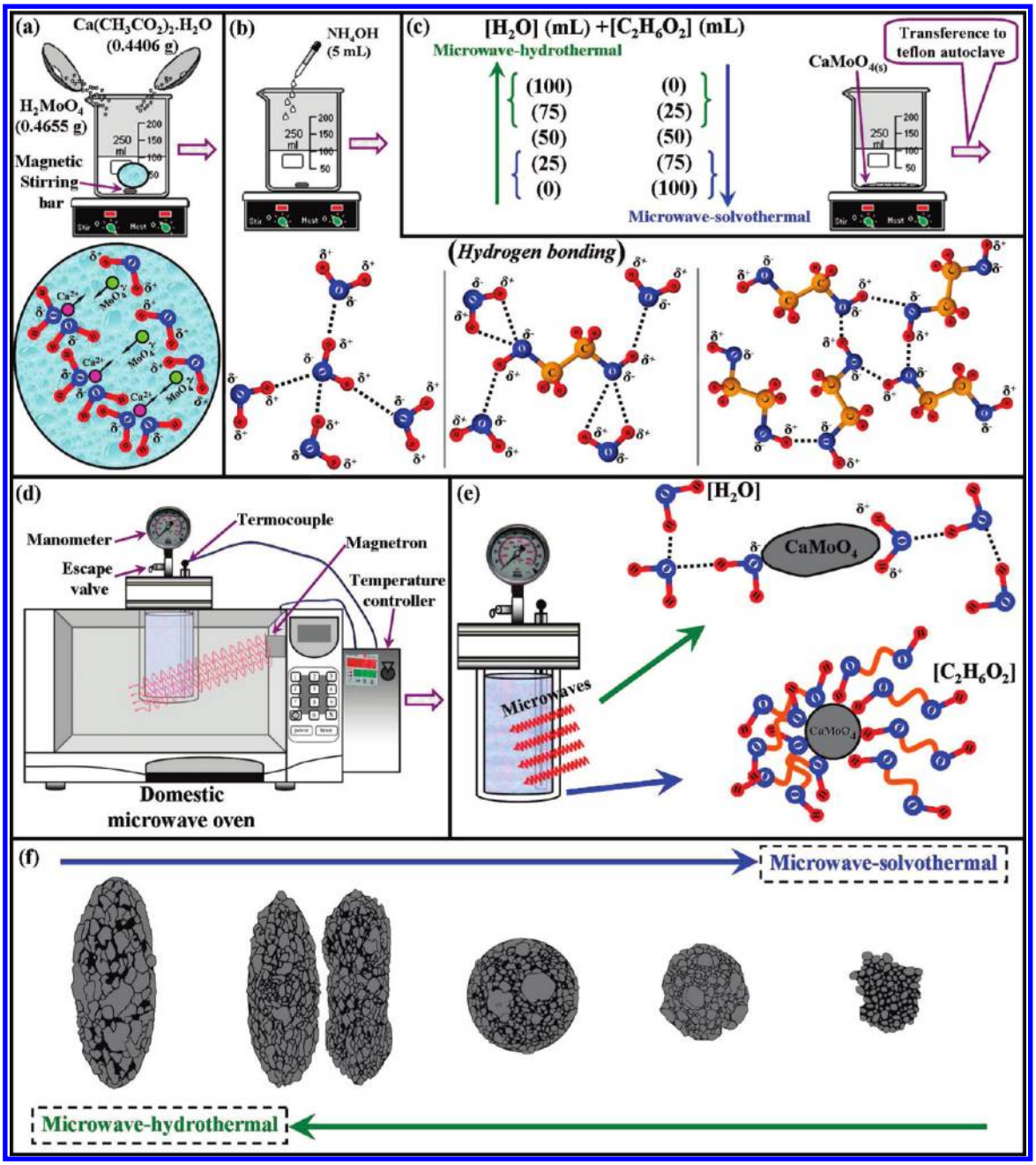

Figure 8. Schematic representation of the synthesis, processing, and growth mechanism of $CaMoO_4$ meso- and nanocrystals: (a) chemical synthesis (solvation and coprecipitation reaction), (b) increase of precipitation rate with NH_4OH and different types of hydrogen bonds between H_2O and/or $C_2H_6O_2$, (c) the different solvent ratios ($H_2O/C_2H_6O_2$) employed in preparation of $CaMoO_4$ meso-/nanocrystals and transference to a Teflon autoclave, (d) domestic microwave-assisted hydrothermal/solvothermal system employed in the processing of $CaMoO_4$ meso-/nanocrystals, (e) increase of the effective collision rates between the nano- and microcrystals with heating by action of the microwave irradiation and possible involvement of solvent molecules on the crystals, causing steric hindrance, orientation, and trapping of small nanocrystals, promoting anisotropic/isotropic growth, and (f) meso-/nanocrystal growth evolution as a function of processing in microwaves with different solvent ratios ($H_2O/C_2H_6O_2$).

nanocrystals can be observed. In the range using from 100 to 75 mL of H_2O as solvent, the microwave-hydrothermal method is used; with 50 mL of H_2O and 50 mL of $C_2H_6O_2$, the solvothermal−microwave−hydrothermal method is used; and in the range using from 100 to 75 mL of $C_2H_6O_2$ as solvent, the solvothermal−hydrothermal method is used. In all the methods employed, the obtained $CaMoO_4$ coprecipitated. After this step, these systems were stirred for 30 min and transferred to the Teflon autoclave. Figure 8d illustrates a schematic representation of the domestic microwave system employed in the processing of the $CaMoO_4$ oriented aggregate crystals and meso- and nanocrystals (see Supporting Information Figure SI-5). This apparatus was developed via several adaptations performed on a domestic microwave oven (model NN-ST357WRPH Piccolo 22 L, Panasonic). In Figure 8e, inside this system, the high frequency of the microwave irradiation interacts with the permanent dipoles of the liquid phases (H_2O and/or $C_2H_6O_2$), which initiates a rapid heating resulting from the resultant molecular rotation. Likewise, permanent or induced dipoles in the dispersed

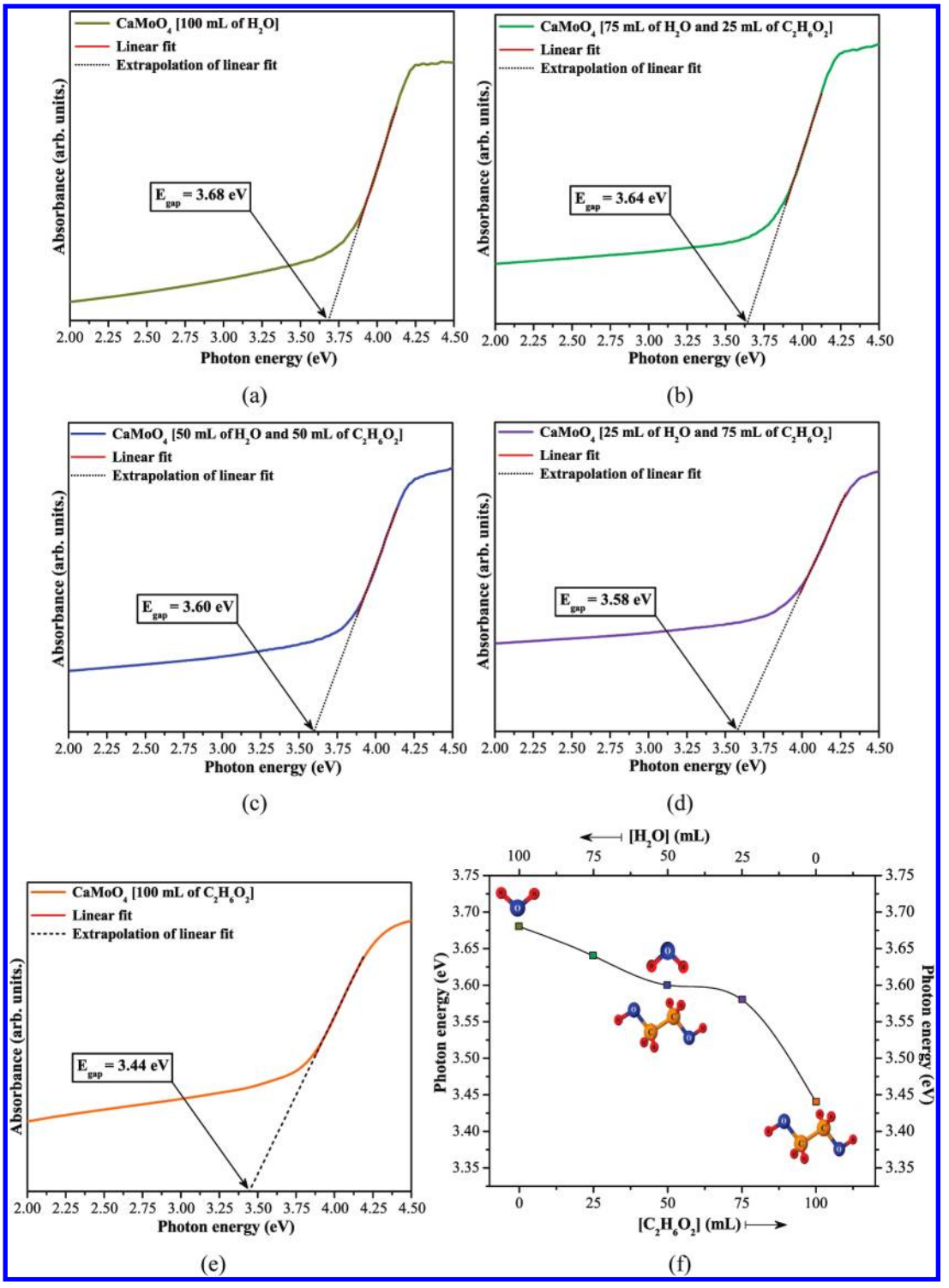

Figure 9. UV−vis absorbance spectra of $CaMoO_4$ crystals prepared with different solvent ratios ($H_2O/C_2H_6O_2$) and processed in a microwave-assisted hydrothermal/solvothermal system: (a) 100 mL of H_2O, (b) 75 mL of H_2O and 25 mL of $C_2H_6O_2$, (c) 50 mL of H_2O and 50 mL of $C_2H_6O_2$, (d) 25 mL of H_2O and 75 mL of $C_2H_6O_2$, (e) 100 mL of $C_2H_6O_2$, and (f) optical band gap values as a function of different solvent ratios.

phase cause a rapid heating of the particles.[90,91] Thus, the microwave irradiation is able to promote the effective collision between the nanoparticles, contributing to growth of the oriented aggregate crystals and meso- and nanocrystals. The adsorption of H_2O and/or $C_2H_6O_2$ on the $CaMoO_4$ nanoparticle surfaces favors the aggregation process by means of the van der Waals interaction of the hydrogen bonds of solvent with the OH groups and polarizations of nearby nanoparticles. Figure 8f illustrates the morphological evolution and anisotropic growth of a $CaMoO_4$ oriented aggregate with the employment of H_2O as solvent and the isotropic growth of $CaMoO_4$ meso- and nanocrystals with the employment of $C_2H_6O_2$ as solvent.[92]

UV−Visible Absorption Spectroscopy Analyses of $CaMoO_4$ Crystals. Parts a−e of Figure 9 show the UV−vis absorbance spectra of $CaMoO_4$ crystals prepared with different

solvent volume ratios ($H_2O/C_2H_6O_2$) and processed in a microwave-assisted hydrothermal/solvothermal system at 140 °C for 1 h, respectively. The found optical band values as a function of different types of solvent ratios are shown in Figure 9f.

The optical band gap energy (E_{gap}) was estimated by the method proposed by Wood and Tauc.[93] According to these authors, the E_{gap} is associated with absorbance and photon energy by the following equation:

$$h\nu\alpha \propto (h\nu - E_{gap})^n \quad (8)$$

where α is the absorbance, h is the Planck constant, ν is the frequency, E_{gap} is the optical band gap and n is a constant associated with the different types of electronic transitions ($n = {}^1/_2, 2, {}^3/_2$, or 3 for direct allowed, indirect allowed, direct forbidden, and indirect forbidden transitions, respectively). The literature explains that the[94] molybdates have an optical absorption process governed by direct electronic transitions. In this phenomenon, the electronic charges located in the maximum-energy states in the valence band (VB) go to the minimum-energy states in the conduction band (CB) after an absorption process but occurring always in the same region of the Brillouin zone.[95] Based on this information, the E_{gap} values of $CaMoO_4$ crystals were calculated using $n = {}^1/_2$ in eq 8. The obtained data are illustrated in Figure 9 and listed in Table 5. In addition, this table also shows a comparison between the E_{gap} obtained in this work and those reported in the literature.[64,96−98]

Table 5. Comparative Results between the Optical Band Gap Energy (Experimental and Theoretical) of $CaMoO_4$ Obtained in This Work and Those Reported in the Literature by Different Synthesis Methods[a]

M	shape	T (°C)	t (h)	E_{gap} (eV)	ref
CP	nanopowders	400	2	5.09	64
CP	nanopowders	500	2	4.87	64
CP	nanopowders	600	2	5.18	64
CP	nanopowders	700	2	5.16	64
CZ	crystal	1400	24	5.0	96
PLA	nanoparticles	900	3	4.70	97
PP	spherical	450	4	2.90	98
PP	spherical	500	4	3.70	98
PP	spherical	600	4	4.20	98
PP	spherical	700	4	4.70	98
MH	corn-cob-like	140	1	3.68	[□]
MH	dumbbell-like	140	1	3.64	[□]
MHS	spherical-like	140	1	3.60	[□]
MS	quasi-spherical-like	140	1	3.58	[□]
MS	nanoparticles	140	1	3.44	[□]
theoretical	displacement	of Mo	(0.0 Å)	4.64	[□]
theoretical	displacement	of Mo	(0.1 Å)	4.49	[□]
theoretical	displacement	of Mo	(0.15 Å)	4.36	[□]
theoretical	displacement	of Mo	(0.2 Å)	4.2	[□]
theoretical	displacement	of Mo	(0.25 Å)	4.02	[□]
theoretical	displacement	of Mo	(0.3 Å)	3.81	[□]
theoretical	displacement	of Mo	(0.35 Å)	3.57	[□]
theoretical	displacement	of Mo	(0.4 Å)	3.47	[□]

[a] M = method; T = temperature; t = time; E_{gap} = optical band gap; CP = complex polymerization; CZ = Czochralski; PLA = pulsed laser ablation; PP = polymeric precursor; MH = microwave-hydrothermal; MHS = microwave-hydrothermal-solvothermal; MS = microwave-solvothermal; [□] = this work.

As can be seen from Table 5, the E_{gap} values of $CaMoO_4$ oriented aggregate crystals and meso- and nanocrystals are smaller than most E_{gap} values of $CaMoO_4$ reported in the literature.[64,96−98] This behavior can be related to the presence of different defect densities on the $CaMoO_4$ prepared by different methods. These preparation methods lead to the obtention of $CaMoO_4$ with different (shape, average crystal size, and structural order−disorder) degrees in the lattice. Therefore, also these factors promoted the formation of intermediary energy levels within the band gap. In our case, the small E_{gap} values found for $CaMoO_4$ oriented aggregate crystals and meso- and nanocrystals can be due to distortions on the lattice caused by microwave irradiation coupled with the [MoO_4] clusters.[99] Also, the modifications of the crystal morphologies by different solvent ratios can lead to the formation of new intermediary electronic states within the band gap.[100]

Band Structures of the Crystalline $CaMoO_4$ Phase without and with Displacements Theoretically Induced on the Mo Atoms. Figure 10 illustrates the calculated band structures of the crystalline $CaMoO_4$ phase without and with displacements performed on Mo atoms. In order to calculate the E_{gap} value corresponding to the distorted lattices, a displacement of 0.35 Å on the Mo atoms was necessary along the x-, y-, and z-axes (0.05 Å, −0.25 Å, and −0.24 Å) into the primitive cell.

The calculated E_{gap} exhibited considerable differences when both the structures were compared. As was expected, the theoretical calculations indicated an E_{gap} of 4.64 eV for the crystalline $CaMoO_4$ phase without the presence of structural defects or distortions (Figure 10a), while in the distorted structure (Mo atom displaced of 0.35 Å) this value was approximately 3.57 eV (Figure 10b). Therefore, these data confirm that this reduction in the E_{gap} is associated with the appearance and redistribution of intermediary energy levels between the valence band (VB) and conduction band (CB)

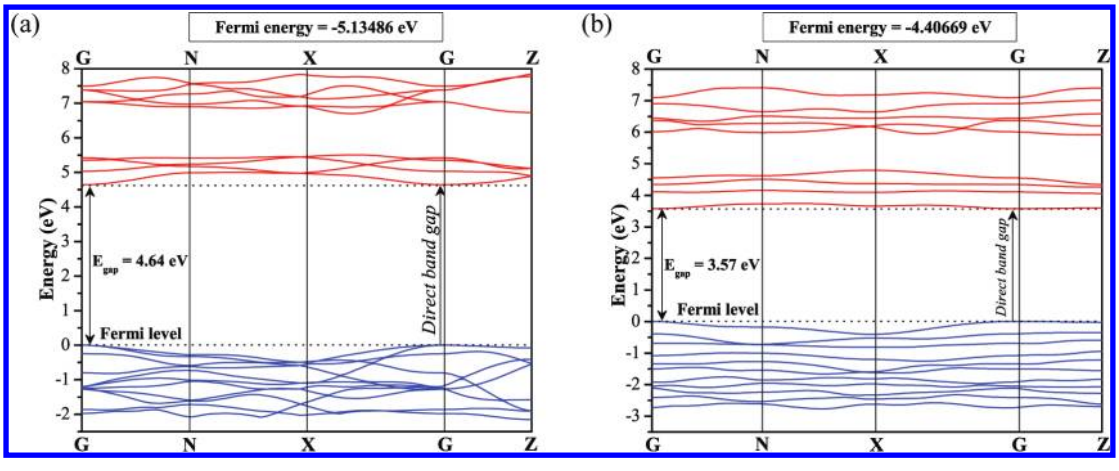

Figure 10. Calculated band structures of the crystalline $CaMoO_4$ phase without (a) and with (b) displacements on the Mo atoms.

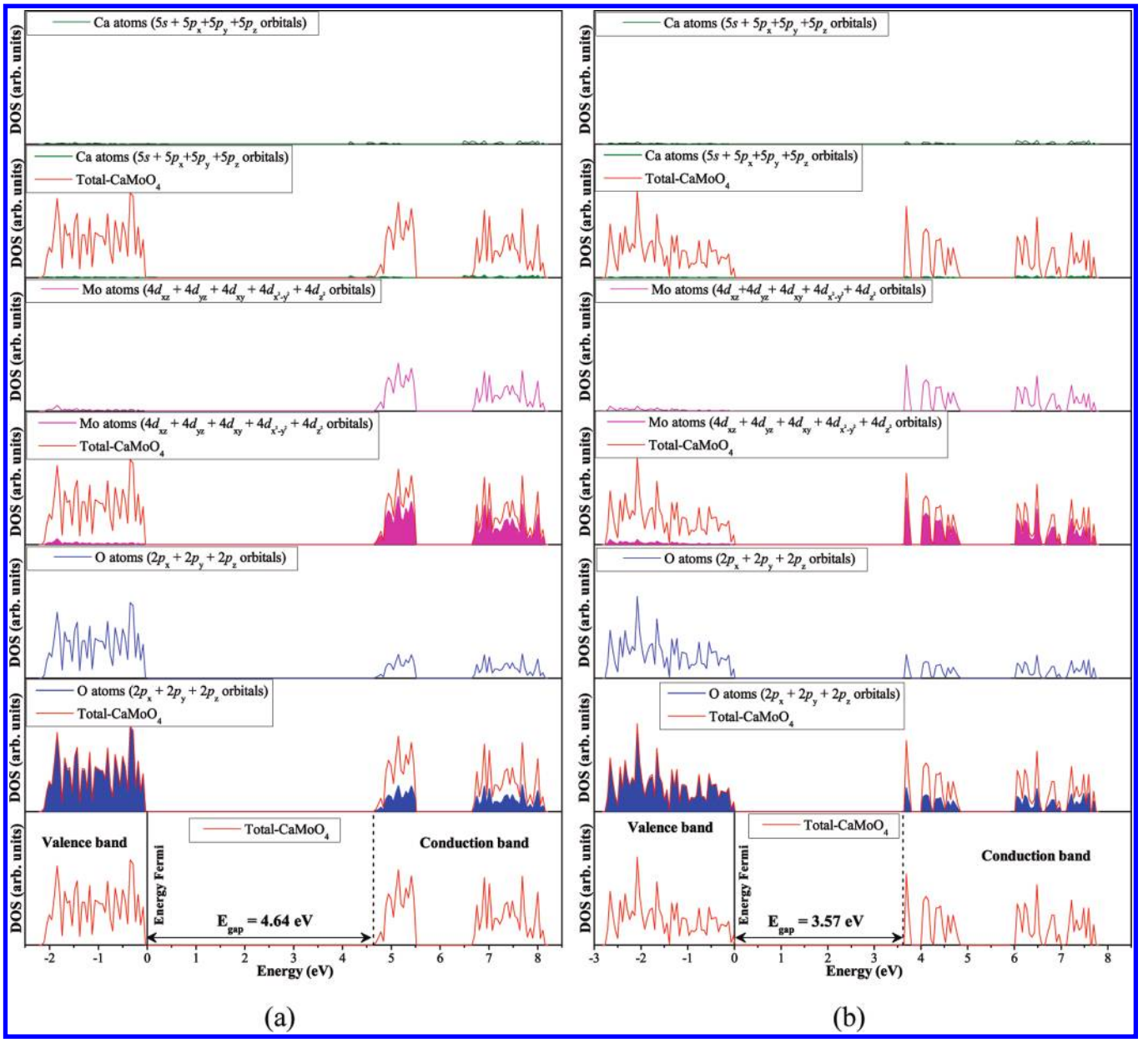

Figure 11. Total DOS of crystalline structure $CaMoO_4$ without (a) and with (b) displacements on the Mo atoms.

(see Figure 10). According to the theoretical calculations, the band structures modeled in both cases indicated a direct electronic transition as a consequence of this physical phenomenon occurring in the same region in the Brillouin zone (G point → G point) (see Supporting Information Figure SI-6). The theoretical results reported in this work showed good agreement with those experimentally obtained (see Table 5 and Supporting Information Figure SI-7).

Density of States for the Crystalline $CaMoO_4$ Structure without and with Displacements Theoretically Induced on the Mo Atoms. Figure 11 shows the density of states (DOS) calculated at the DFT level for crystalline $CaMoO_4$ without and with displacement on the Mo atoms, promoting distortions into the $[MoO_4]$ clusters, respectively.

In Figure 11 it was noted that the DOS of crystalline structure $CaMoO_4$ without (a) and with (b) displacement on the Mo atoms has the VB predominantly composed of oxygen (O) $2p_x$, $2p_y$, and $2p_z$ atomic orbitals, while the CB is mainly formed of molybdenum (Mo) $4d_{xy}$, $4d_{xz}$, $4d_{yz}$, $4d_{x^2-y^2}$, and $4d_{z^2}$ atomic orbitals. As can be observed in Figure 11a, the calcium (Ca) 5s, $5p_x$, $5p_y$, and $5p_z$ atomic orbitals have a minimal contribution (between −3 and 9 eV) due to a weak hybridization between the Ca and O orbitals. Also, the total DOS of all orbitals for the $CaMoO_4$ showed that those arising from the Ca atoms have few contributions between the intermediary energy states because of the ionic character of its chemical bond (Ca−O) (see Figure 11b and Supporting Information Figure SI-8 and 9). The Mo 4d atomic orbitals present two different types of energy levels. The projected individual DOS of each Mo atomic orbital revealed that the CB is basically constituted of $4d_{x^2-y^2}$ and $4d_{z^2}$ orbitals (from 4.64 to 5.51 eV) as well as $4d_{xy}$, $4d_{xz}$, and $4d_{yz}$ atomic orbitals (from 6.65 to 8.15 eV) (see Supporting Information Figure SI-8). In principle, the theoretical data suggested a strong hybridization between the O 2p (above the VB) and Mo 4d orbitals (near the CB), respectively. After displacement of 0.35 Å caused on the Mo atoms, a significant change in the DOS was noted, consequently reducing the

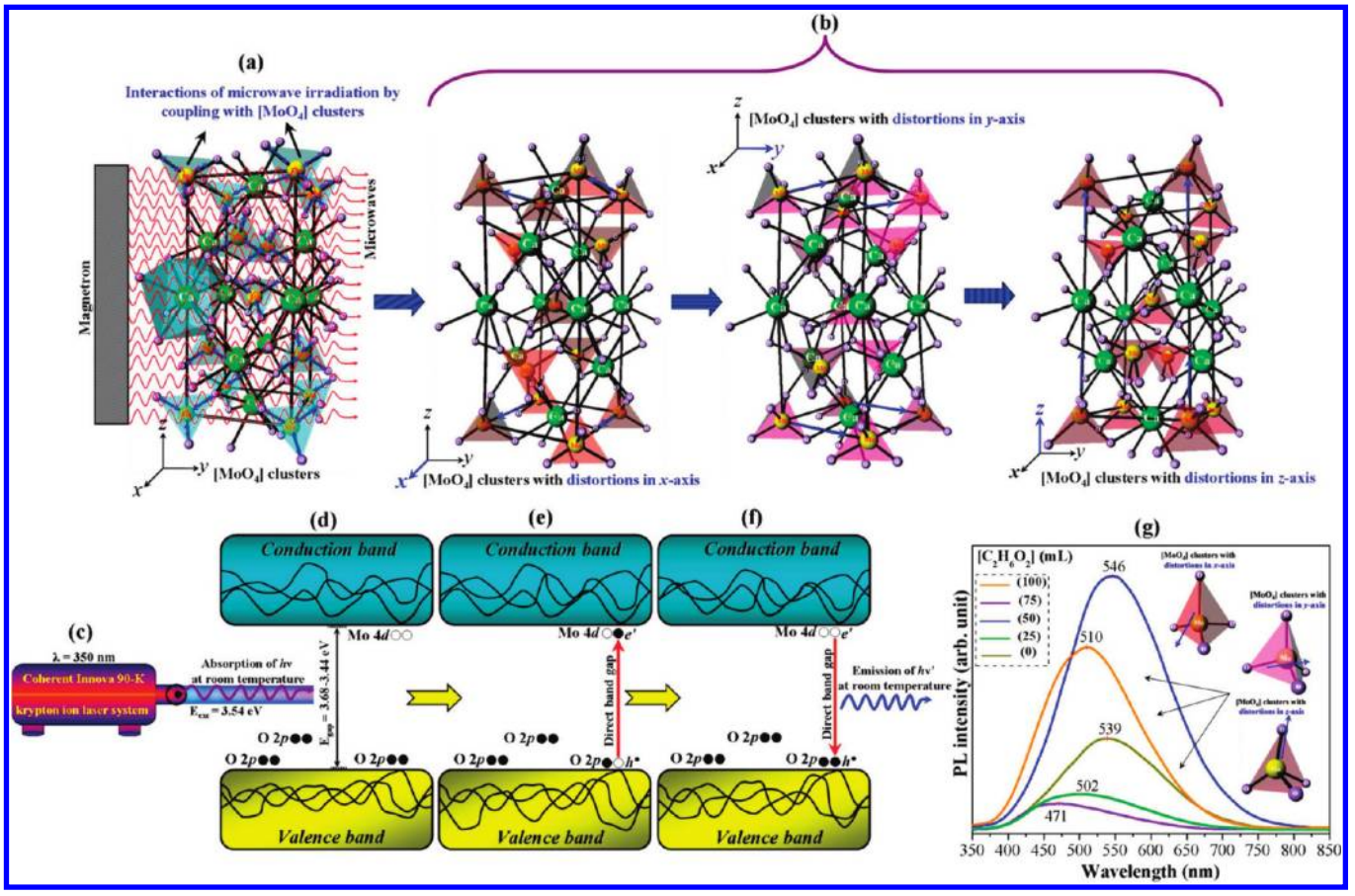

Figure 12. (a) Schematic representation of the unit cell under microwave irradiation, (b) possible distortion sets on the $[MoO_4]$ clusters into the lattice caused by coupling with microwave irradiation, (c) wavelength employed in the excitation process of $CaMoO_4$ meso- and nanocrystals, (d) proposed wide band model before excitation with the presence of intermediary energy levels, (e) electronic transition from oxygen 2p orbitals (lower energy levels) to molybdenum 4d orbitals (higher energy levels) by absorption of ($h\nu$) at room temperature, (f) emission process of photons ($h\nu'$) because of the radiative return processes of electrons situated at molybdenum 4d orbitals to oxygen 2p orbitals, and (g) PL spectra of $CaMoO_4$ meso- and nanocrystals prepared with different solvent ratios ($H_2O/C_2H_6O_2$). Inset shows the distorted MoO_4 clusters in the x, y, and z axes.

E_{gap} (3.57 eV). Figure 11b illustrates the reorganization of the intermediary energy levels in the valence ($2p_x$, $2p_y$, and $2p_z$) and conduction ($4d_{xy}$, $4d_{xz}$, $4d_{yz}$, $4d_{x^2-y^2}$, and $4d_{z^2}$) bands. In this distorted $CaMoO_4$ lattice, the O atoms are more distant from those of Mo atoms (see also Supporting Information Figure SI-9).

Photoluminescence Properties Analyses: Distortions on the $[MoO_4]$ Clusters in the Lattice by Microwave Irradiation and a Wide Band Model. In the last years, the experimental and theoretical results reported in the literature have tried to explain the possible mechanisms responsible for the PL properties of molybdates.[101−108] Blasse,[101] Chandrasekhar, and White[102] explained the PL emissions of $CaMoO_4$ by means of a model containing both metal and ligand orbitals. In this model, the charge transfer processes in these orbitals were considered the key factors for the origin of this optical property. Mikhailik et al.[103,104] interpreted the PL properties of $CaMoO_4$ as a radiative recombination of electron−hole pairs localized into the MoO_4^{2-} groups. Liu et al.[105] and Lei et al.[106] reported that the charge-transfer transitions into the $[MoO_4]^{2-}$ complex can be considered the main reason for the green PL emissions of $CaMoO_4$. Recently, Thongtem et al.[107] attributed the PL emission of $CaMoO_4$ nanopowders with $^1T_2 \rightarrow {}^1A_1$ electronic transitions to the MoO_4^{2-} anions, which can be treated as excitons. However, all these explanations are directly associated with the MoO_4^{2-} groups (ions), but the $CaMoO_4$ is a crystalline solid composed of interconnected clusters (...$[MoO_4]$−$[CaO_8]$−$[MoO_4]$...). Therefore, in our work, we assume that the tetrahedral $[MoO_4]$ clusters can be distorted because the Mo atoms have good interactions with microwave irradiation.[108] As there is an interconnection of the $[MoO_4]$ and $[CaO_8]$ clusters in the tetragonal structure, it is possible to conclude that any distortion caused on the $[MoO_4]$ cluster also promotes a slight deformation of the Ca−O bonds. However, the ionic nature (radial character) exhibited by the $[CaO_8]$ clusters prevents a high degree of distortions on them (see Figure 2 and Supporting Information Figures SI-5, 8, and 9). These distortions are able to induce a symmetry break in the lattice, leading to the appearance of intermediate levels within the band gap. Also, other factors, such as inhomogeneous crystal size distribution, the crystallographic orientation of crystals, and changes in morphology (see Supporting Information Figure SI-5), can promote a charge gradient and polarization on the crystal surfaces, causing the formation of these intermediate levels that are necessary for recombination processes (electron−hole) and favoring PL emission at room temperature in $CaMoO_4$ oriented aggregate crystals and meso- and nanocrystals.

Figure 12 shows the representation for the $CaMoO_4$ unit cell, possible distortion sets on the $[MoO_4]$ clusters, laser excitation, a wide band model, and the PL spectrum of

$CaMoO_4$ oriented aggregate crystals and meso- and nanocrystals prepared with different solvent ratios ($H_2O/C_2H_6O_2$) and processed in a microwave-assisted hydrothermal/solvothermal system at 140 °C for 1 h.

Inside the autoclave cell, the high frequency of the microwave irradiation may also interact with the lattice of the $CaMoO_4$ crystal solid (Figure 12a). It is reported by Rao et al.[108] that Mo atoms are known to couple strongly to microwave irradiation at ordinary temperatures; this coupling generates high heating inside the lattice, which can lead to deformation/strain in the $CaMoO_4$ lattice; some of these possible distortions on the tetrahedron [MoO_4] clusters were simulated through displacements on the Mo atoms along the axes (*x*, *y*, and *z*) illustrated in Figure 12b. Therefore, this structural distortion leads to formation of intermediary energy levels within the band gap. Figure 12c shows the laser employed in excitation of $CaMoO_4$ meso-/nanocrystals. The wavelength energy (350 nm $\approx$ 3.543 eV) is able to excite several electrons localized in intermediary energy levels within the band gap (Figure 12d). These direct electronic transitions in band gap occur in the same region of the Brillouin zone between the maximum-energy states near to minimum-energy states (see Figure 10). During the excitation process at room temperature, some electrons localized at lower intermediary energy levels (oxygen 2p orbitals) near the valence band absorb the photon energies ($h\nu$) at this wavelength. As a consequence of this phenomenon, the energetic electrons are promoted to higher intermediary energy levels (molybdenum 4d orbitals) located near the conduction band (Figure 12e). When the electrons fall back to lower energy states, again via radiative return processes, the energies arising from this electronic transition is converted to photons ($h\nu'$) (Figure 12f). In this case, several photons ($h\nu'$), originating from the participation of different energy states during the electronic transitions, are responsible for the broad PL spectra (Figure 12g). As can be observed in Figure 12, the PL emission maximum also is influenced by the morphology of the crystals, depending on the shape and arrangement of clusters having different types of defects in surface and lattice. Since the distortion on the tetrahedral [MoO_4] clusters leads to specific defects at medium range, causing a nonlinear PL behavior, according to Yin et al.,[109] the PL intensity in a $CaMoO_4$ nanostructure may greatly depend on the particle distribution. These authors have demonstrated that the improvement in PL intensity of $CaMoO_4$ can be related with the control of the particle size distribution and the homogeneity of particle morphology. Our results indicated that the spherical-like $CaMoO_4$ mesocrystals with isotropic growth present the largest intensities of PL emission. Thus, we believe that PL behavior can also be influenced by effective control of the orientation of these crystals. However, the true factor that acts on the PL behavior is not still completely clear, and future investigations based on both experimental data and theoretical calculations will be necessary for a better understanding of the origin of this optical property.

Conclusions

In summary, $CaMoO_4$ oriented aggregate crystals and meso- and nanocrystals were obtained with solvent ratios (water/ethylene glycol) and processed in a microwave-assisted hydrothermal/solvothermal system at 140 °C for 1 h. XRD patterns and FT-Raman spectra indicated that the $CaMoO_4$ meso- and nanocrystals are ordered at long- and short-range with the presence of a scheelite-type tetragonal structure without the presence of secondary phases. FT-IR spectra showed characteristic vibrational modes of a tetragonal crystal system. FEG-SEM micrographs indicated an anisotropic growth for $CaMoO_4$ oriented aggregate crystals processed under hydrothermal-microwave conditions and isotropic growth for $CaMoO_4$ meso- and nanocrystals processed under solvothermal-microwave conditions. Thus, the micrographs indicated that the solvent ratios are able to influence the crystal growth process, and also, the micrographs showed the agglomerate nature and polydisperse size distribution. TEM micrographs revealed that the presence of different solvent ratios (water/ethylene glycol) promotes the formation of $CaMoO_4$ oriented aggregate crystals and meso- and nanocrystals. HR-TEM micrographs evidenced that the $CaMoO_4$ oriented aggregate crystals are formed by aggregating of nanocrystals in the same crystallographic plane, but not all those nanocrystals are oriented, while, in $CaMoO_4$ mesocrystals, all the nanocrystals are oriented, as seen by the SAED. HR-TEM micrographs evidenced that the $CaMoO_4$ nanocrystals present preferential growth along the [001] direction, but in general, these nanocrystals have different crystallographic orientations, as also seen by the SAED. A possible growth mechanism for the formation of $CaMoO_4$ oriented aggregate and meso- and nanocrystals prepared with different solvent ratios and a processed microwave-assisted hydrothermal/solvothermal system was explained in detail. UV−vis absorption spectra showed different optical band gap values, which were associated with the presence of intermediary energy levels within the band gap, which are basically composed of oxygen 2p orbitals (above the valence band) and molybdenum 4d orbitals (below the conduction band). The DFT investigations performed on the band structures suggested that the direct electronic transitions (G−G) occur in the band gap. The DOS analyses indicated that the valence band is mainly formed of oxygen $2p_x$, $2p_y$, $2p_z$ atomic orbitals, while the conduction band is composed mainly of molybdenum atoms containing $4d_{xy}$, $4d_{xz}$, $4d_{yz}$, $4d_{x^2-y^2}$, and $4d_{z^2}$ atomic orbitals. Also, the band structures and the DOS estimated by the theoretical calculations showed that the electronic states are influenced by the displacements performed on the Mo atoms (lattice formers) in the [MoO_4] clusters, while little influence is noted by Ca atoms (lattice modifier) in the [CaO_8] clusters due to 5s, $5p_x$, $5p_y$, and $5p_z$ atomic orbitals presenting weak hybridization with the oxygen atomic orbitals. The PL emission maximum can be linked to crystal shape/intrinsic defects in the surface and mainly to possible distortions on the tetrahedron [MoO_4] clusters in the lattice caused by the microwave irradiation. Moreover, the nonlinear PL behavior also can be related to formation of defects at medium range in the lattice caused by the magnetic field oscillator of the microwave irradiation by coupling with solvents and/or the crystal lattice, that leads to obtention of (oriented aggregate crystals, meso and nanocrystals) with different crystallographic orientations.

Acknowledgment. The authors acknowledge the financial support of the Brazilian research financing institutions: FAPESP (No . 2009/50303-4), CNPq, and CAPES. Special thanks are extended to Prof. Dr. D. Keyson and Dr. D. P. Volanti for the development of the domestic microwave−hydrothermal system.

Supporting Information Available: Figures showing the viscosities of different solvent ratios ($H_2O/C_2H_6O_2$) employed in preparation of $CaMoO_4$ crystals; the specific surface area of $CaMoO_4$ aggregated oriented crystals and meso- and nanocrystals; N_2 adsorption−desorption isotherms of $CaMoO_4$ aggregated oriented crystals and meso- and nanocrystals; TEM/HR-TEM micrographs and SAED of $CaMoO_4$ oriented aggregate crystals and meso- and nanocrystals; a schematic representation of a $CaMoO_4$ oriented aggregate crystals and meso- and nanocrystals and possible relation of orientation of crystals with the photoluminescence properties; a diagram of the primitive body-centered-tetragonal Brillouin zone; the correlation of the experimental gap energy [E_{gap}(exp)] with the theoretical gap energy [E_{gap}(theo)] after the displacement of Mo atoms to deform the $CaMoO_4$ crystal; and partial and total DOS for each one of the main atomic orbitals involved (Ca = 5s, 5p, Mo = 4d, and O = 2p) of crystalline $CaMoO_4$ with and without displacement of the Mo atoms. This material is available free of charge via the Internet at http://pubs.acs.org.

References

(1) (a) Thongtem, T.; Phuruangrat, A.; Thongtem, S. *Mater. Lett.* **2008**, *62*, 454–457. (b) Sun, Y.; Ma, J.; Jiang, X.; Fang, J.; Song, Z.; Gao, X.; Liu, Z. *Solid State Sci.* **2010**, *12*, 1283–1286.

(2) (a) Cui, C.; Bi, J.; Gao, D. *Appl. Surf. Sci.* **2008**, *255*, 3463–3465. (b) Gao, D.; Lai, X.; Cui, C.; Cheng, P.; Bi, J.; Lin, D. *Thin Solid Films* **2010**, *518*, 3151–3155.

(3) Farabaugh, E. N.; Peiser, H. S.; Wachtman, J. B., Jr. *J. Res. Natl. Bur. Stand.* **1966**, *70A*, 379–384.

(4) Zhang, Y.; Holzwarth, N. A. W.; Williams, R. T. *Phys. Rev. B* **1998**, *57*, 12738–12750.

(5) Achary, S. N.; Patwe, S. J.; Mathews, M. D.; Tyagi, A. K. *J. Phys. Chem. Solids* **2006**, *67*, 774–781.

(6) Cavalli, E.; Bovero, E.; Belletti, A. *J. Phys.: Condens. Matter* **2002**, *14*, 5221–5228.

(7) Li, X.; Yang, Z.; Guan, L.; Guo, J.; Wang, Y.; Guo, Q. *J. Alloys Compd.* **2009**, *478*, 684–686.

(8) Balakshy, V. I.; Asratyan, K. R.; Molchanov, V. Y. *J. Opt. A: Pure Appl. Opt.* **2001**, *3*, S87–S92.

(9) Andrade, L. H. C.; Li, M..S.; Guyot, Y.; Brenier, A.; Boulon, G. *J. Phys.: Condens. Matter* **2006**, *18*, 7883–7892.

(10) Kiss, Z. J.; Pressley, R. J. *Appl. Opt.* **1996**, *5*, 1474–1486.

(11) Xie, A.; Yuan, X.; Hai, S.; Wang, J.; Wang, F.; Li, L. *J. Phys. D.: Appl. Phys.* **2009**, *42*, 105107–105113.

(12) Bavykina, I.; Angloher, G.; Hauff, D.; Kiefer, M.; Petricca, F.; Pröbst, F. *Opt. Mater.* **2009**, *31*, 1382–1387.

(13) Choi, G. K.; Kim, J. R.; Yoon, S. H.; Hong, K. S. *J. Eur. Ceram. Soc.* **2007**, *27*, 3063–3067.

(14) Choi, G. K.; Cho, S. Y.; An, J. S.; Hong, K. S. *J. Eur. Ceram. Soc.* **2006**, *26*, 2011–2015.

(15) Haque, M. M.; Lee, H. I.; Kim, D. K. *J. Alloys Compd.* **2009**, *481*, 792–796.

(16) Liang, Y.; Han, X.; Yi, Z.; Tang, W.; Zhou, L.; Sun, J.; Yang, S.; Zhou, Y. *J. Solid State Electrochem.* **2007**, *11*, 1127–1131.

(17) Belogurov, S.; Kornoukhov, V.; Annenkov, A.; Borisevich, A.; Fedorov, A.; Korzhik, M.; Ligoun, V.; Missevitch, O.; Kim, S. K.; Kim, S. C.; Kim, S. Y.; Kwak, J. W.; Lee, H. S.; Lee, J.; Myung, S. S.; Lee, M. J.; Kim, Y. D.; Lee, J. Y.; Lee, J. I.; Kim, H. J.; Kwon, Y. J.; Hwang, M. J.; Zhu, J. J. *IEEE Trans. Nucl. Sci.* **2005**, *52*, 1131–1135.

(18) Annenkov, A. N.; Buzanov, O. A.; Danevich, F. A.; Georgadze, A. Sh.; Kim, S. K.; Kim, H. J.; Kim, Y. D.; Kobychev, V. V.; Kornoukhov, V. N.; Korzhik, M.; Lee, J. I.; Missevitch, O.; Mokina, V. M.; Nagorny, S. S.; Nikolaiko, A. S.; Poda, D. V.; Podviyanuk, R. B.; Sedlak, D. J.; Shkulkova, O. G.; So, J. H.; Solsky, I. M.; Tretyak, V. I.; Yurchenko, S. S. *Nucl. Instrum. Methods Phys. Res., Sect. A.* **2008**, *584*, 334–345.

(19) Woo, S. I.; Kim, J. S.; Jun, H. K. *J. Phys. Chem. B* **2004**, *108*, 8941–8946.

(20) Yan, S.; Zhang, J.; Zhang, X.; Lu, S.; Ren, X.; Nie, Z.; Wang, X. *J. Phys. Chem. C* **2007**, *111*, 13256–13260.

(21) Hou, Z.; Chai, R.; Zhang, M.; Zhang, C.; Chong, P.; Xu, Z.; Li, G.; Lin, J. *Langmuir* **2009**, *25*, 12340–12348.

(22) Yoon, J. W.; Ryu, J. H.; Shim, K. B. *Mater. Sci. Eng. B* **2006**, *127*, 154–158.

(23) Mikhailik, V. B.; Kraus, H.; Miller, G.; Mykhaylyk, M. S.; Wahl, D. *J. Appl. Phys.* **2005**, *97*, 083523–083530.

(24) Mikhailik, V. B.; Kraus, H.; Itoh, M.; Iri, D.; Uchida, M. *J. Phys.: Condens. Matter* **2005**, *17*, 7209–7218.

(25) Ryu, J. H.; Yoon, J. W.; Lim, C. S.; Oh, W. C.; Shim, K. B. *J. Alloys Compd.* **2005**, *390*, 245–249.

(26) Marques, A. P. A.; Longo, V. M.; de Melo, D. M. A.; Pizani, P. S.; Leite, E. R.; Varela, J. A.; Longo, E. *J. Solid State Chem.* **2008**, *181*, 1249–1257.

(27) Campos, A. B.; Simões, A. Z.; Longo, E.; Varela, J. A.; Longo, V. M.; de Figueiredo, A. T.; De Vicente, F. S.; Hernandes, A. C. *Appl. Phys. Lett.* **2007**, *91*, 051923–051925.

(28) Komarneni, S.; Roy, R.; Li, Q. H. *Mater. Res. Bull.* **1992**, *27*, 1393–1405.

(29) Thongtem, T.; Phuruangrat, A.; Thongtem, S. *Curr. Appl. Phys.* **2008**, *8*, 189–197.

(30) Floriano, W. B.; Nascimento, M. A. C. *Braz. J. Phys.* **2004**, *34*, 38–41.

(31) Cavalcante, L. S.; Sczancoski, J. C.; Tranquilin, R. L.; Varela, J. A.; Longo, E.; Orlandi, M. O. *Particuology* **2009**, *7*, 353–362.

(32) Brunauer, S.; Emmett, P. H.; Teller, E. *J. Am. Chem. Soc.* **1938**, 309–319.

(33) Becke, A. D. *J. Chem. Phys.* **1993**, *98*, 5648–5652.

(34) Lee, C.; Wang, W.; Parr, R. G. *Phys. Rev. B* **1988**, *37*, 785–789.

(35) Cora, F.; Alfredsson, M.; Mallia, G.; Middlemiss, D. S.; Mackrodt, W.; Dovesi, R.; Orlando, R. *Struct. Bonding* (*Berlin*); Springer Verlag: Berlin, 2004; p 113.

(36) http://www.crystal.unito.it/BasisSets/Ptable.html.

(37) Dovesi, R.; Saunders, V. R.; Roetti, C.; Orlando, R.; Zicovich Wilson, C. M.; Pascale, F.; Civalleri, B.; Doll, K.; Harrison, N. M.; Bush, I. J.; Arco, P. D.; Llunell, M. *CRYSTAL06 User's Manual*; University of Torino: 2006.

(38) Kokalj, A. *J. Mol. Graph.* **1999**, *17*, 176–179.

(39) Joint Committee on Powder Diffraction Standards 2001; Diffraction Data File No. 29-0351; International Centre for Diffraction Data (ICDD, formerly JCPDS): Newtown Square, PA.

(40) Holland, T. J. B.; Redfern, S. A. T. *Mineral. Mag.* **1997**, *61*, 65–77.

(41) Gong, Q.; Qian, X.; Ma, X.; Zhu, Z. *Cryst. Growth Des.* **2006**, *6*, 1821–1825.

(42) Kim, J. G.; Choi, J. H.; Jeong, J. M.; Kim, Y. M.; Suh, I. H.; Kim, J. P.; Kim, Y. J. *Bull. Korean Chem. Soc.* **2007**, *28*, 391–396.

(43) Marques, A. P. A.; Leite, E. R.; Varela, J. A.; Longo, E. *Nanoscale Res. Lett.* **2008**, *3*, 152–157.

(44) Wang, J.; Jing, X.; Yan, C.; Lin, J.; Liao, F. *J. Electrochem. Soc.* **2005**, *152*, G534–G536.

(45) Sczancoski, J. C.; Bomio, M. D. R.; Cavalcante, L. S.; Joya, M. R.; Pizani, P. S.; Varela Longo, E.; Li, M. S.; Andrés, J. *J. Phys. Chem. C* **2009**, *113*, 5812–5822.

(46) Sczancoski, J. C.; Cavalcante, L. S.; Marana, N. L.; da Silva, R. O.; Tranquilin, R. L.; Joya, M. R.; Pizani, P. S.; Varela, J. A.; Sambrano, J. R.; Li, M. S.; Longo, E.; Andrés, J. *Curr. Appl. Phys.* **2010**, *10*, 614–624.

(47) http://www.jcrystal.com/steffenweber/JAVA/JSV/jsv.html.

(48) http://dor.huji.ac.il/3d_finds.html.

(49) Senyshyn, A.; Kraus, H.; Mikhailik, V. B.; Vasylechko, L.; Knapp, M. *Phys. Rev. B.* **2006**, *73*, 014104–014113.

(50) http://polyhedra.org/poly/show/0/tetrahedron.

(51) http://polyhedra.org/poly/show/128/snub_disphenoid.

(52) Porto, S. P. S.; Scott, J. F. *Phys. Rev.* **1967**, *157*, 716–719.

(53) Christofilos, D.; Kourouklis, G. A.; Ves, S. *J. Phys. Chem. Solids* **1995**, *56*, 1122–1129.

(54) Sarantopoulou, E.; Raptis, C.; Ves, S.; Christofilos, D.; AKourouklis, G. *J. Phys.: Condens. Matter* **2002**, *14*, 8925–8938.

(55) Scott, J. F. *J. Chem. Phys.* **1968**, *48*, 874–876.

(56) Basiev, T. T.; Sobol, A. A.; Voronko, Y. K.; Zverev, P. G. *Opt. Mater.* **2000**, *15*, 205–216.

(57) Basiev, T. T.; Sobol, A. A.; Zverev, P. G.; Ivleva, L. I.; Osiko, V. V.; Powell, R. C. *Opt. Mater.* **1999**, *11*, 307–314.

(58) Rousseau, D. L.; Bauman, R. P.; Porto, S. P. S. *J. Raman Spectrosc.* **1981**, *10*, 253–290.

(59) Barker, A. S., Jr. *Phys. Rev.* **1964**, *135*, A742–A747.

(60) Golubović, A.; Gajić, R.; Dohćević-Mitrović, Z.; Nikolić, S. *J. Alloys Compd.* **2006**, *415*, 16–22.

(61) Ling, Z. C.; Xia, H. R.; Ran, D. G.; Liu, F. Q.; Sun, S. Q.; Fan, J. D.; Zhang, H. J.; Wang, J. Y.; Yu, L. L. *Chem. Phys. Lett.* **2006**, *426*, 85–90.

(62) Zverev, P. G. *Phys. Status Solidi C* **2004**, *1*, 3101–3105.

(63) Sarantopoulou, E.; Raptis, C.; Ves, S.; Christofilos, D.; Kourouklis, G. A. *J. Phys.: Condens. Matter* **2002**, *14*, 8925–8938.

(64) Marques, A. P. A.; Motta, F. V.; Leite, E. R.; Pizani, P. S.; Varela, J. A.; Longo, E.; de Melo, D. M. A. *J. Appl. Phys.* **2008**, *104*, 043505–043510.

(65) Tarte, P.; Liegeois-Duyckaerts, M. *Spectrochim. Acta, Part A* **1972**, *28*, 2029–2036.
(66) Clark, G. M.; Doyle, W. P. *Spectrochim. Acta, Part A* **1966**, *22*, 1441–1447.
(67) Lei, F.; Yan, B. *J. Solid State Chem.* **2008**, *181*, 855–862.
(68) Li, G.; Wang, Z.; Quan, Z.; Li, C.; Lin, J. *Cryst. Growth Des.* **2007**, *7*, 1797–1802.
(69) Cavalcante, L. S.; Sczancoski, J. C.; Tranquilin, R. L.; Joaya, M. R.; Pizani, P. S.; Varela, J. A.; Longo, E. *J. Phys. Chem. Solids* **2008**, *69*, 2674–2680.
(70) Penn, R. L.; Banfield, J. F. *Science* **1998**, *281*, 969–971.
(71) Lu, W. G.; Fang, J. Y. *J. Phys. Chem. B* **2005**, *109*, 19219−19222.
(72) Chen, D.; Tang, K.; Li, F.; Zheng, H. *Cryst. Growth Des.* **2006**, *6*, 247–252.
(73) Zhou, L.; O'Brien, P. *Small* **2008**, *4*, 1566–1574.
(74) Xu, C.; Zou, D.; Guo, H.; Jie, F.; Ying, T. *J. Lumin.* **2009**, *129*, 474–477.
(75) Lee, J. S.; Choi, S. C. *J. Eur. Ceram. Soc.* **2005**, *25*, 3307–3314.
(76) Komarneni, S.; Katsuki, H. *Pure Appl. Chem.* **2002**, *74*, 1537–1543.
(77) Thongtem, T.; Phuruangrat, A.; Thongtem, S. *J. Nanopart. Res.* **2010**, *12*, 2287–2294.
(78) Zhao, X.; Li, T. K.; Xi, Y. Y.; Ng, D. H. L.; Yu, J. *Cryst. Growth Des.* **2006**, *6*, 2210–2213.
(79) Penn, R. L. *J. Phys. Chem. B* **2004**, *108*, 12707–12712.
(80) Geng, X.; Liu, L.; Jiang, J.; Yu, S. H. *Cryst. Growth Des.* **2010**, *10*, 3448–3453.
(81) Ye, F.; Peng, Y.; Chen, G. Y.; Deng, B.; Xu, A. W. *J. Phys. Chem. C* **2009**, *113*, 10407–10415.
(82) Yu, J. G.; Zhao, X. F.; Liu, S. W.; Li, M.; Mann, S.; Ng, D. H. L. *Appl. Phys. A: Mater. Sci. Process.* **2007**, *87*, 113–120.
(83) Emsley, J. *Chem. Soc. Rev.* **1980**, *9*, 91–124.
(84) Omta, A. W.; Kropman, M. F.; Woutersen, S.; Bakker, H. J. *Science* **2003**, *301*, 347–349.
(85) Bushuev, Y. G. *Russian Chem. Bull.* **1997**, *46*, 888–891.
(86) Rozhkova, A. G.; Butyrskaya, E. V.; Rozhkova, M. V.; Shaposhnik, V. A. *J. Struct. Chem.* **2007**, *48*, 166–169.
(87) Zhang, J. B.; Zhang, P. Y.; Ma, K.; Han, F.; Chen, G. H.; Wei, X. H. *Sci. China, Ser. B: Chem.* **2008**, *51*, 420–426.
(88) Kao, M. J.; Tien, D. C.; Jwo, C. S.; Tsung, T. T. *J. Phys. Conf. Ser.* **2005**, *13*, 442–445.
(89) Zwirbla, W.; Sikorska, A.; Linde, B. B. J. *J. Mol. Struct.* **2005**, *743*, 49–52.
(90) Murugan, A. V.; Samuel, V.; Ravi, V. *Mater. Lett.* **2006**, *60*, 479–480.
(91) Phuruangrat, A.; Thongtem, T.; Thongtem, S. *J. Cryst. Growth* **2009**, *311*, 4076–4081.
(92) Wang, W.; Hu, Y.; Goebl, J.; Lu, Z.; Zhen, L.; Yin, Y. *J. Phys. Chem. C* **2009**, *113*, 16414–16423.
(93) Wood, D. L.; Tauc, J. *Phys. Rev. B* **1972**, *5*, 3144–3151.
(94) Lacomba-Perales, R.; Ruiz-Fuertes, J.; Errandonea, D.; Martínez-García, D.; Segura, A. *Eur. Phys. Lett.* **2008**, *83*, 37002–37006.
(95) Longo, V. M.; Orhan, E.; Cavalcante, L. S.; Porto, S. L.; Espinosa, J. W. M.; Varela, J. A.; Longo, E. *Chem. Phys.* **2007**, *334*, 180–188.
(96) Zakharko, Y.; Luchechko, A.; Syvorotka, I.; Stryganyuk, G.; Solskii, I. *Radiat. Meas.* **2010**, *45*, 429–431.
(97) Ryu, J. H.; Choi, B. G.; Yoon, J. W.; Shima, K. B.; Machi, K.; Hamada, K. *J. Lumin.* **2007**, *124*, 67–70.
(98) Longo, V. M.; de Figueiredo, A. T.; Campos, A. B.; Espinosa, J. W. M.; Hernandes, A. C.; Taft, C. A.; Sambrano, J. R.; Varela, J. A.; Longo, E. *J. Phys. Chem. A* **2008**, *112*, 8920–8928.
(99) Jackson, S. K.; Layland, R. C.; Loye, H. C. Z. *J. Alloys Compd.* **1999**, *291*, 94–101.
(100) Fujita, M.; Itoh, M.; Takagi, S.; Shimizu, T.; Fujita, N. *Phys. Status Solidi B* **2006**, *243*, 1898–1907.
(101) Blasse, G. *J. Solid State Chem.* **1975**, *13*, 339–344.
(102) Chandrasekhar, B. K.; White, W. B. *Mater. Res. Bull.* **1990**, *25*, 1513–1518.
(103) Mikhailik, V. B.; Kraus, H.; Wahl, D.; Mykhaylyk, M. S. *Phys. Status Solidi B* **2005**, *242*, R17–R19.
(104) Mikhailik, V. B.; Kraus, H.; Itoh, M.; Iri, D.; Uchida, M. *J. Phys.: Condens. Matter* **2005**, *17*, 7209–7218.
(105) Liu, J.; Huang, X.; Li, Y.; Li, Z. *J. Mater. Chem.* **2007**, *17*, 2754–2758.
(106) Lei, H.; Zhang, S.; Zhu, X.; Sun, Y.; Fu, Y. *Mater. Lett.* **2010**, *64*, 344–346.
(107) Phuruangrat, A.; Thongtem, T.; Thongtem, S. *J. Alloys Compd.* **2009**, *481*, 568–572.
(108) Rao, K. J.; Vaidhyanathan, B.; Ganguli, M.; Ramakrishnan, P. A. *Chem. Mater.* **1999**, *11*, 882–895.
(109) Yin, Y.; Gao, Y.; Sun, Y.; Zhou, B.; Ma, L.; Wu, X.; Zhang, X. *Mater. Lett.* **2009**, *64*, 602–604.